Astron. Astrophys. 358, 257–275 (2000)

ASTRONOMY AND ASTROPHYSICS

SO and CS observations of molecular clouds⋆

II. Analysis and modelling of the abundance ratios – probing O_2/CO with SO/CS?

A. Nilsson[1], **Å. Hjalmarson**[1], **P. Bergman**[1], **and T.J. Millar**[2]

[1] Onsala Space Observatory, 439 92 Onsala, Sweden
[2] Department of Physics, UMIST, P.O. Box 88, Manchester M60 1QD, UK

Received 24 August 1999 / Accepted 14 March 2000

Abstract. We here analyse the observational SO and CS data presented in Nilsson et al. (2000). The SO/CS integrated intensity ratio maps are presented for 19 molecular clouds, together with tables of relevant ratios at strategic positions, where we have also observed ^{34}SO and/or C^{34}S. The SO/CS abundance ratio as calculated from an LTE analysis is highly varying within and between the sources. Our isotopomer observations and Monte Carlo simulations verify that this is not an artifact due to optical depth problems. The variation of the maximum SO/CS abundance ratio between the clouds is 0.2–7. The largest variations within a cloud are found for the most nearby objects, possibly indicating resolution effects. We have also performed time dependent chemical simulations. We compare the simulations with our observed SO/CS abundance ratios and suggest a varying oxygen to carbon initial abundance, differing temporal evolution, density differences and X–ray sources associated with young stellar objects as possible explanations to the variations. In particular, the observed variation of the maximum SO/CS abundance ratio between the clouds can be explained by using initial O/C$^+$ abundance ratios in the range 1.3–2.5. We finally derive a relationship between the SO/CS and O_2/CO abundance ratios, which may be used as a guide to find the most promising interstellar O_2 search targets.

Key words: ISM: clouds – ISM: molecules – ISM: abundances – ISM: structure

1. Introduction

For a long time it has been a commonly accepted idea that the SO/CS abundance ratio may probe evolutionary effects in molecular clouds. The present project started in 1996 and is based upon this idea, together with our hope that these investigations may be used to guide searches for interstellar O_2 by the SWAS (Melnick et al. 1997) and Odin (Hjalmarson 1997; Nordh 1997) satellites and also may lead to a better understanding of the presence, or absence, of O_2 at detectable levels. The reason for this is the similarity between the dominant formation and destruction mechanisms for SO and O_2 in dense interstellar clouds, viz,

$$\begin{array}{l} \mathrm{OH + O \rightarrow O_2 + H} \\ \mathrm{OH + S \rightarrow SO + H} \end{array} \quad (1)$$

$$\begin{array}{l} \mathrm{O_2 + C \rightarrow CO + O} \\ \mathrm{SO + C \rightarrow CS + O} \\ \mathrm{SO + C \rightarrow CO + S} \end{array} \quad (2)$$

and

$$\mathrm{O_2 + S \rightarrow SO + O} \quad (3)$$

Therefore we expect that the abundances of SO and O_2 will remain low, because of the efficient loss reactions, Eq. (2), as long as the C abundance remains high. Only when C has been "locked up" by the formation of CO, will the SO and O_2 abundances become high, i.e. at "late times". CS, on the other hand, reaches a high abundance level already at "early times". This behaviour has been clearly demonstrated by time dependent chemical models, e.g. by Bergin et al. (1995), Bergin & Langer (1997), El–Nawawy et al. (1997), and Taylor et al. (1998). The same behaviour is also found in models which use enhanced ion–dipole rate coefficients at low temperatures (cf. Lee et al. 1996).

Already Langer et al. (1984) demonstrated by means of chemical modelling the dramatic influence of the initial C/O elemental abundance ratio on the O_2 concentration. The many failures to detect interstellar O_2 [e.g. the recent low gas phase limits by Combes et al. (1997); Maréchal et al. (1997a); Olofsson et al. (1998); Melnick et al. (1999) and references therein] then may be explained by an elevated C/O ratio, somewhat above the commonly used ratio of about 0.4. Recently Maréchal et al. (1997b) have reported an extensive study on the chemistry and emissivity of O_2 in interstellar clouds. They predict O_2 abundances and emissivities in several O_2 transitions for varying cloud conditions and confirm the conclusion by Langer et al. (1984) that the initial C/O abundance ratio very strongly influences the O_2 abundance. Until recently dedicated observational

Send offprint requests to: Å. Hjalmarson

⋆ Table 1 and Figs. 4 to 21 are only available in electronic form at the CDS via anonymous ftp to cdsarc.u-strasbg.fr (130.79.128.5) or via http://cdsweb.u-strasbg.fr/Abstract.html)

Correspondence to: hjalmar@oso.chalmers.se

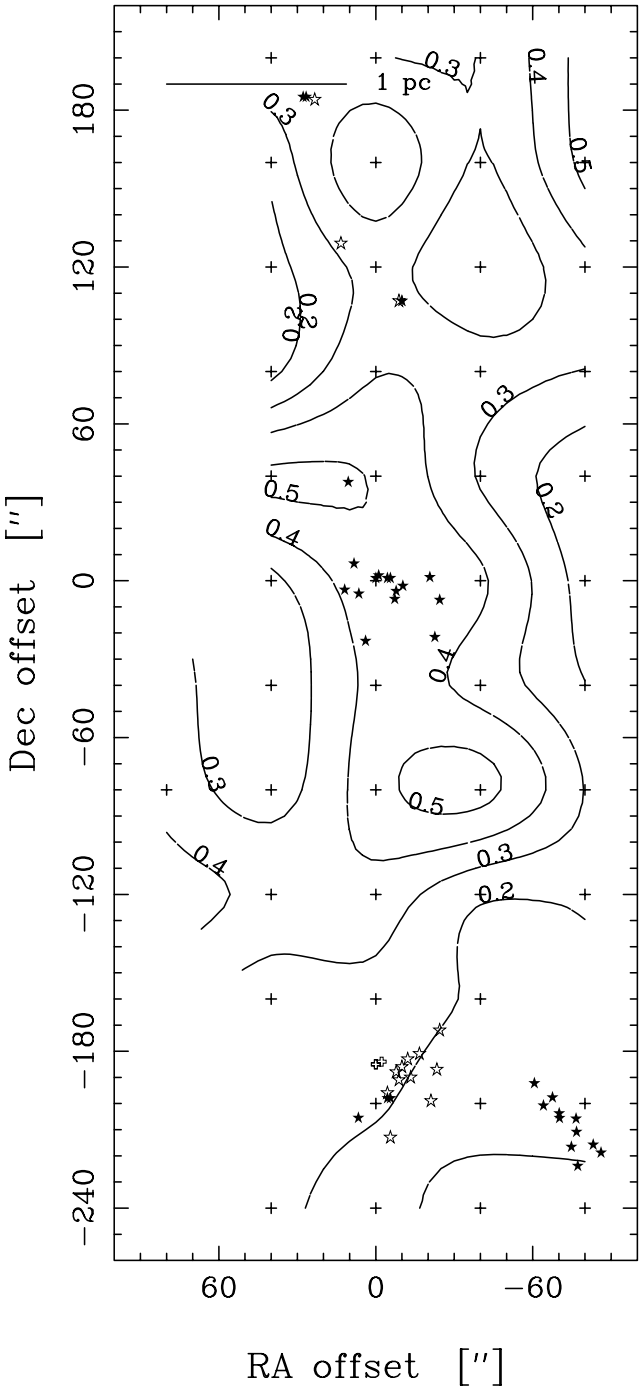

Fig. 1a. The SO/CS integrated intensity ratio in DR 21(OH). Observed positions are marked with a cross (+). Various objects from the SIMBAD database have been entered, see Table 1

studies determining the eventual variations of the SO/CS abundance ratio within and between molecular clouds have been rather rare (e.g. Swade 1989a, 1989b; Heithausen et al. 1998; Bergin et al. 1997; Pratap et al. 1997). Gerin et al. (1997) have observed chemical inhomogeneities in high latitude and dark clouds and also have performed chemical modelling. These authors advocate that in some clouds chemical bistability caused by a high ionization phase, in addition to the usually adopted low ionization phase, may play a role (cf. also Le Bourlot et al. 1995).

In this paper we analyse SO($J_N = 3_2 - 2_1$) and CS($J = 2 - 1$) observational data resulting from extensive mapping of 19 molecular clouds performed with the Onsala 20 m telescope (Nilsson et al. 2000; hereafter Paper I). In Sect. 2 we present integrated intensity ratio maps, and tabulate relevant ratios between SO, ^{34}SO, CS and C^{34}S, together with the estimated SO/CS abundance ratios. In the subsequent Sect. 3 we present results from astrochemistry simulations. In Sect. 4 we discuss our observational findings in terms of the astrochemistry modelling results, and in Sect. 5 we summarize our findings and draw some main conlusions.

In a subsequent Paper III (Olofsson et al., in prep.) we will combine the present data (available in Paper I) with newly acquired C^{18}O(1–0) maps. In this way we can discuss the actual SO and CS abundance variations (rather than the SO/CS abundance ratio) across and between the sources treated in this paper in the light of chemical modelling.

Table 1. SIMBAD objects and sign captions as displayed in the ratio maps, Figs. 1a–1v

2. Observational results, subsequent data processing, and analysis

The source coordinates are, together with distance estimates, catalogued in Table 1 of Paper I. Moreover, the observational procedures, data reduction, and observational results have been described in Paper I. The observing strategy was to map the SO($3_2 - 2_1$) line until the signal disappeared and subsequently make CS($2 - 1$) maps. We also observed C^{34}S($2 - 1$) and ^{34}SO($3_2 - 2_1$) in strategic positions. We mapped the C^{34}S($2 - 1$) and ^{34}SO($3_2 - 2_1$) lines in the very clear case of variations in NGC 1333.

2.1. Integrated intensity ratio maps

The SO($3_2 - 2_1$) and CS($2 - 1$) integrated intensities and 1 σ errors were calculated and tabulated for all positions where both lines had been observed. As a measure of the 1 σ uncertainty of the ratio $R = A/B$ we use

$$\Delta R = R\sqrt{(\Delta A/A)^2 + (\Delta B/B)^2}$$

where ΔA and ΔB are the 1 σ errors in A and B, respectively. Our acceptance criterion for a "reliable" ratio was set to $\Delta R < 0.25R$ (4 σ). However, this strong criterion could not be applied to the NGC 1333 rare isotopomer data for which a 3 σ limit was used. The ratios are presented as ratio maps in Figs. 1a–1v. Here we have also included physical size scales together with selected objects from the SIMBAD database. The SIMBAD objects presented in Figs. 1a–1v are X–ray and IR sources, masers, HII regions and HH–objects (see Table 1 for

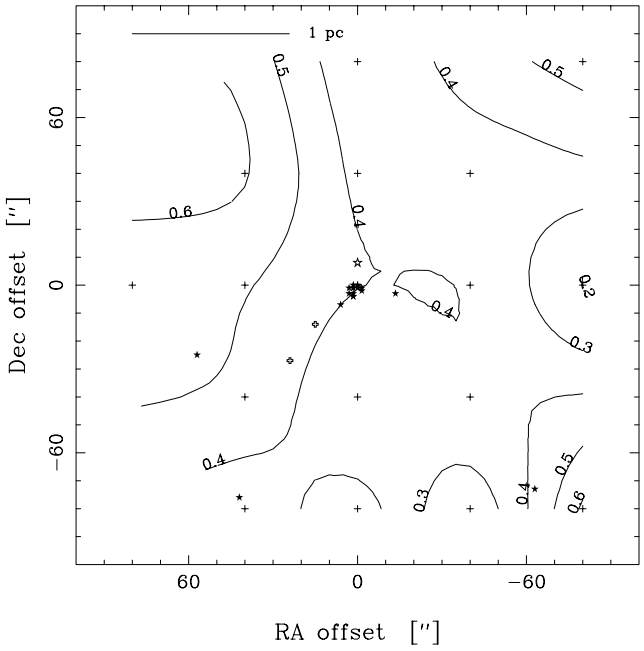

Fig. 1b. The SO/CS integrated intensity ratio in G 34.3+0.2

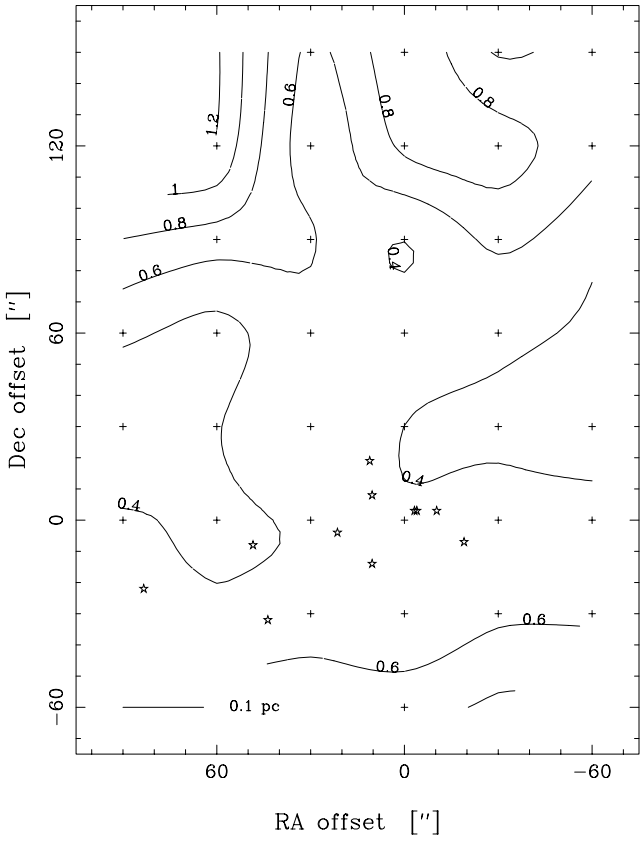

Fig. 1d. The SO/CS integrated intensity ratio in NGC 1333

Fig. 1c. The SO/CS integrated intensity ratio in IRAS 21391+5802

symbol explanations). The contour maps in Figs. 1a–1v have been displayed using bicubic interpolation of the contour lines.

Considerable variations in the SO/CS integrated intensity ratio have been found within as well as between the sources. In some sources this ratio exhibits very large variations while in others the variations are small. The maximum and minimum ratios have been tabulated for each map in Table 2.

As explained in Paper I, we have removed a broad gaussian outflow component from the CS($2-1$) and SO(3_2-2_1) line profile maps of NGC 2071 and Orion A. In Orion A an additional component due to the hot core emission was removed. In the integrated intensity ratio maps (Figs. 1j–1k and Figs. 1n–1o) and in Table 2, we present results for both these sources with as well as without removal of an outflow component.

2.1.1. NGC 1333

In NGC 1333 we observe a highly varying SO/CS ratio. In the main isotopomer ratio map (Fig. 1d) we found a very low ratio of about 0.25 at the driving source of the HH 7–11 outflow SVS 13 (Liseau et al. 1988), while the position of the highest ratio of 1.3 coincides with the strong far infrared source IRAS 4 (Jennings et al. 1987). We also see an elevated ratio in an extended region north of IRAS 4. In the ^{34}SO/C^{34}S isotopomer ratio map we confirm, within the current error limits, the main features of the main isotopomer ratio map, using optically thin lines. No kinematical outflow evidence in terms of line–wings is apparent in the observed SO(3_2-2_1) and CS($2-1$) lines. Hence, the strong enhancement of the SO/CS abundance ratio is intrinsic to the quiescent gas although the probable reason for this enhancement is compression caused by the outflow from SVS 13, as will be argued in our subsequent discussion (Sect. 4.1.1). Chernin et

Table 2. Maxima and minima of SO/CS integrated intensity ratios

Source	Max position		Max	Min position		Min
	$\Delta\alpha('')$	$\Delta\delta('')$	Ratio	$\Delta\alpha('')$	$\Delta\delta('')$	Ratio
DR 21(OH)	−80	160	0.53	−80	40	0.13
G 34.3+0.2	−80	−80	0.62	−80	0	0.20
IRAS 21391+5802	60	120	1.17	90	30	0.25
Mon R2	0	0	0.25	0	−40	0.11
NGC 1333	120	−160	1.30	−40	40	0.20
NGC 1333 isotopomers	160	−120	1.69	0	0	0.08
NGC 2024	40	120	0.53	−40	40	0.18
NGC 2068	120	−80	1.26	−40	−40	0.09
NGC 2071	−160	120	1.58	0	40	0.26
Residual NGC 2071	−200	160	1.79	0	0	0.20
NGC 2264IR	0	80	0.77	0	−120	0.26
NGC 7538	40	0	0.65	−40	−160	0.23
OMC–2	0	40	0.30	−40	0	0.10
OMC–3	0	40	0.76	80	−80	0.27
S 140	80	−80	0.68	80	−40	0.13
W3(IRS4)	−80	80	0.73	20	20	0.19
W3(OH)	80	0	0.50	20	60	0.18
W 49N	0	0	0.76	−80	0	0.15
W 51N	120	40	0.69	120	−80	0.20
NGC 2023	−80	−40	0.89	0	0	0.22
Orion A	0	0	3.31	40	120	0.09
Residual Orion A	40	−40	0.34	−40	80	0.03

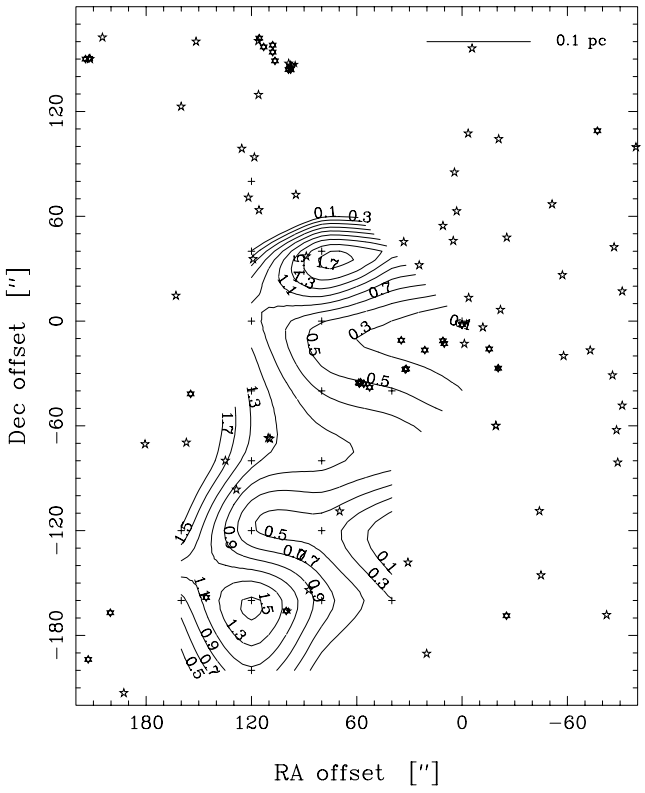

Fig. 1e. The ^{34}SO/C^{34}S integrated intensity ratio in NGC 1333

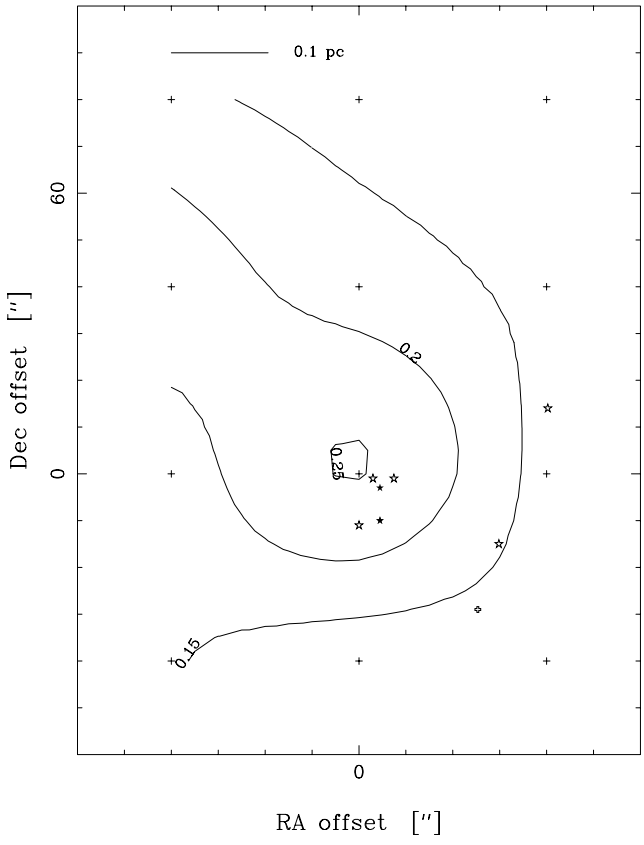

Fig. 1f. The SO/CS integrated intensity ratio in Mon R2

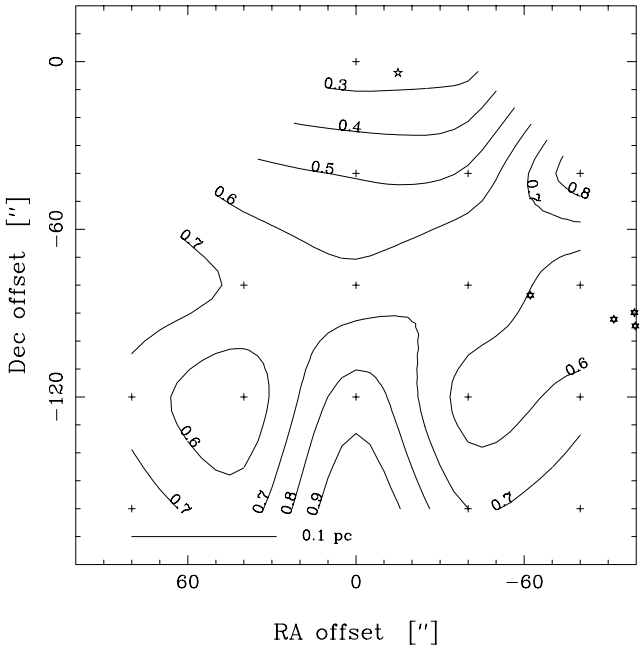

Fig. 1g. The SO/CS integrated intensity ratio in NGC 2023

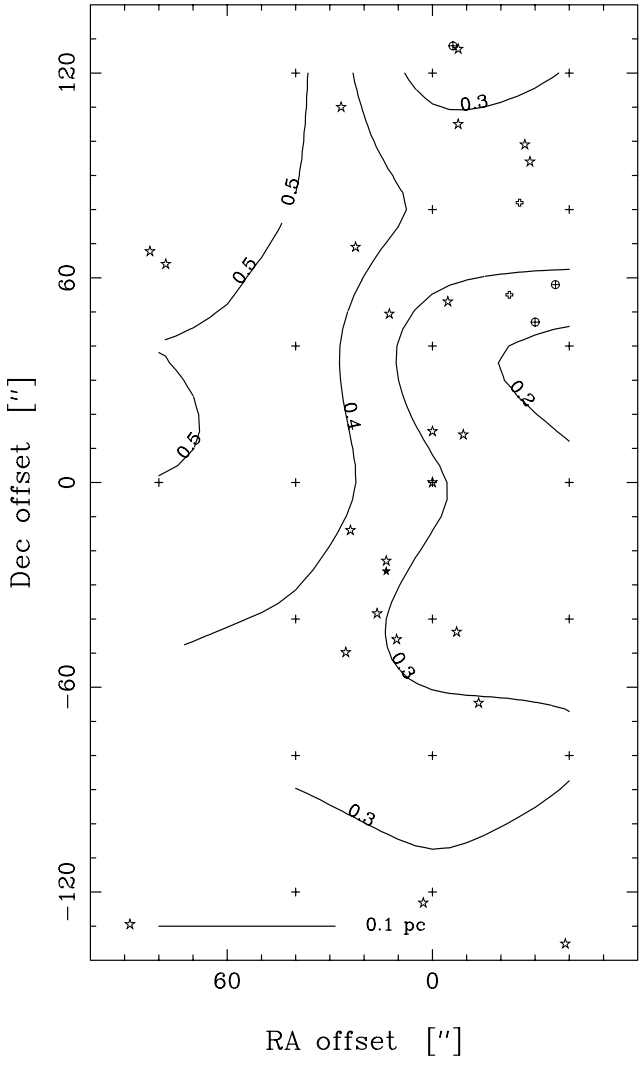

Fig. 1h. The SO/CS integrated intensity ratio in NGC 2024

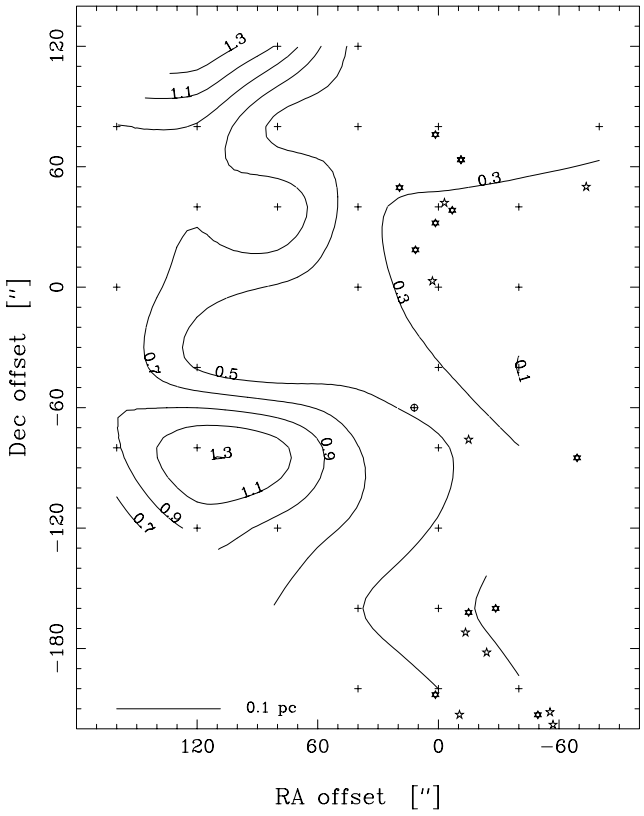

Fig. 1i. The SO/CS integrated intensity ratio in NGC 2068

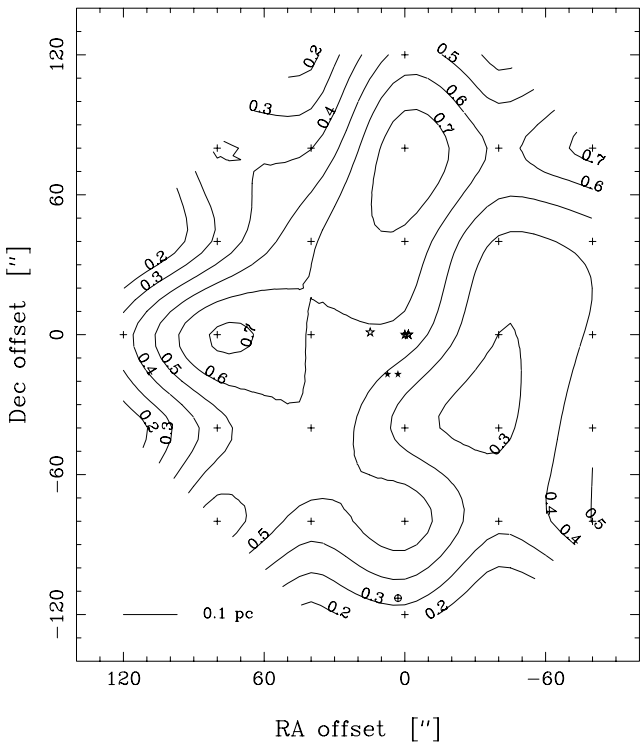

Fig. 1j. The SO/CS integrated intensity ratio in NGC 2071, outflow component included

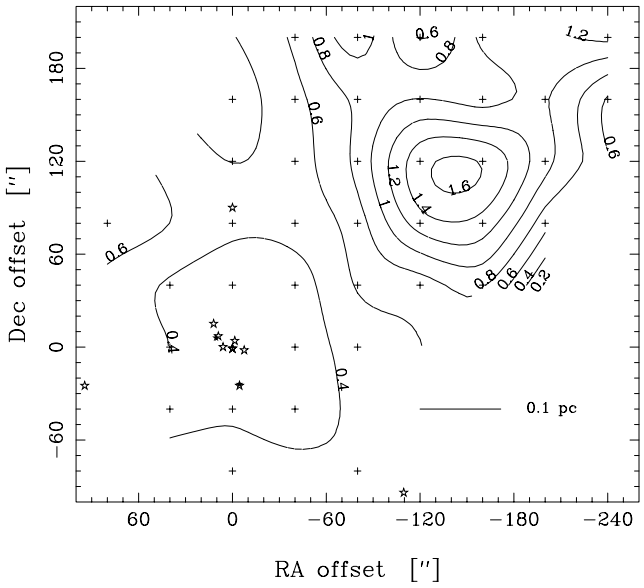

Fig. 1k. The SO/CS integrated intensity ratio in NGC 2071, with a gaussian outflow component removed

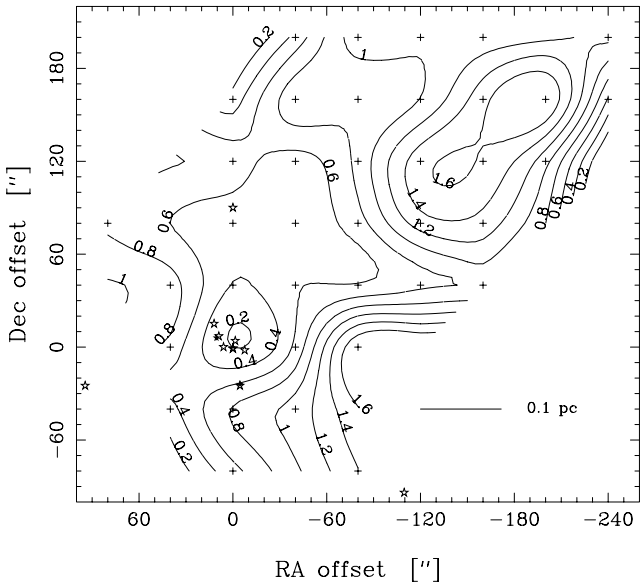

Fig. 1l. The SO/CS integrated intensity ratio in NGC 2264IR

al. (1994) have noted that the SO($3_2 - 2_1$) transition does not (easily) probe the outflowing gas, while the higher excitation SO($6_5 - 5_4$) line is a useful outflow tracer.

2.1.2. NGC 2068

The (0,0) position in our map (Fig. 1i) coincides with the Herbig Haro object HH 24 and the area mapped contains two molecular outflows (Snell & Edwards 1982; Edwards & Snell 1984). The SO/CS ratio maximum of about 1.3 is located in the outflow area between HH 24 and HH 27. Our observed SO and CS distributions are rather clumpy (see Paper I), but the SO and CS "brightness clumps" do not coincide and no kinematic evidence of outflows is apparent in our data. It may well be that the SO/CS ratio maximum in the quiescent gas coincides with a compressed region caused by the "CO outflows". We will return to an analysis of this source in Paper III.

2.1.3. NGC 2071

In NGC 2071 (Fig. 1k) the lowest SO/CS ratio (0.25) appears close to the origin of a very extended outflow source oriented in the NE/SW direction (Snell et al. 1984b; Chernin et al. 1994). The maximum SO/CS ratio (1.6) appears NW of the outflow and results from an increase of the SO emission together with a decrease of the CS emission (see Paper I). This does not indicate a compression by the outflow and we see at present no obvious physical reason for the increased SO/CS ratio. We will return to this question in Paper III.

2.1.4. Orion A

Orion A contains a well–known outflow in our map centre position (e.g. Olofsson et al. 1982; Friberg 1984; Sutton et al. 1995).

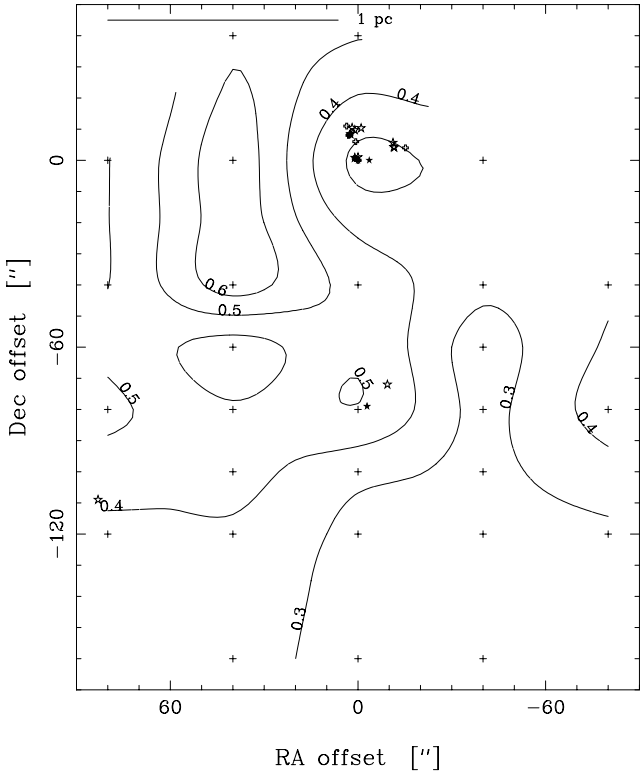

Fig. 1m. The SO/CS integrated intensity ratio in NGC 7538

The SO emission is extremely enhanced in the outflow (see Paper I and Friberg 1984). The broad gaussian outflow component has an SO/CS integrated intensity ratio of about 6 in the centre position. The quiescent cloud (the remaining emission when the outflow and hot core components have been removed, Fig. 1o) has a very low SO/CS integrated intensity ratio (0.03–0.34) – among the lowest found in our sample of molecular clouds.

2.1.5. IRAS 21391+5802

In IRAS 21391+5802 we observe an elevated SO/CS ratio north of map centre position (Fig. 1c). This source contains two outflows (Patel et al. 1995), which are both located near the SO/CS ratio peak.

2.2. Correlation with SIMBAD objects

In Figs. 1a–1v we have displayed a number of SO/CS integrated intensity ratio maps, where also selected objects from the SIMBAD database have been entered (see Table 1 for symbol explanations). However, unfortunately we see no obvious correlation between the SIMBAD objects and the observed variations in the SO/CS ratio.

2.3. From intensity to abundance ratios

Table 3 contains a number of relevant ratios at positions where we have at least three observed lines. The integrated intensity isotopomer ratios (SO/^{34}SO and CS/C^{34}S) provide information about the optical depth. Fig. 2 displays the main line optical depth as a function of the main line to isotopomer intensity ratio, assuming a ^{32}S/^{34}S abundance ratio of 22 (Wilson & Rood 1994; Lucas & Liszt 1998) and the same excitation temperature for both isotopomers. SO/^{34}SO or CS/C^{34}S ratios well below 22 are indicative of optically thick main isotopomer lines. The SO/CS ratio has been included in Table 3 for comparison, with the ratio of the optically thin lines ^{34}SO and C^{34}S. The latter lines will lead to a more reliable estimate of the abundance ratio. In the penultimate column of Table 3 we have entered the ratio considered to be the most reliable ratio, i.e. the ratio derived from the observational data after an optical depth correction. We have here compensated for the assumed isotopic ratio ^{32}S/^{34}S = 22. See the footnotes of Table 3 for further explanations.

Following Irvine et al. (1987) we have subsequently calculated the [SO]/[CS] ratios *assuming optically thin lines* as stated below, and entered the results in the last column of Table 3.

Using the relationship between the observed intensity integrated across the spectral line, $I = \int T_{\rm mb} dv$, and the upper state column density of the transition, N_u, derived by Irvine et al. (1987), for optically thin emission and ignoring the background brightness, we arrive at the following expression for the ratio between the upper state column densities

$$\frac{N_u(\mathrm{SO})}{N_u(\mathrm{CS})} = \left(\frac{\nu_{\mathrm{SO}}}{\nu_{\mathrm{CS}}}\right)^2 \times \frac{A_{\mathrm{CS}}}{A_{\mathrm{SO}}} \times \frac{I_{\mathrm{SO}}}{I_{\mathrm{CS}}}, \quad (4)$$

where ν and A are the frequencies and spontaneous emission rates of the observed transitions. Here all quantities have been properly identified as belonging to SO or CS. The above relationship may be understood as the ratio between the number of photons spontaneously emitted from the upper to the lower SO and CS states in question, and will remain a good approximation if the SO and CS excitation temperatures are similarly large (cf. Irvine et al. 1987). Excitation temperatures of similar size would be expected from the SO($3_2 - 2_1$) and CS($2 - 1$) transitions because of their very similar upper state energies (E_u = 9.23 and 7.05 K, respectively) and A-coefficients (1.15×10^{-5} and 1.68×10^{-5} s^{-1}). The relatively large A-coefficients imply that both transitions are mainly probing gas of high H_2 density, $\gtrsim 10^5$ cm^{-3} (Snell et al. 1984a; Mundy et al. 1986).

Since the total molecular column density N may be related to the upper state column density via

$$N = N_u Q(T) \exp[E_u/kT]/g_u, \quad (5)$$

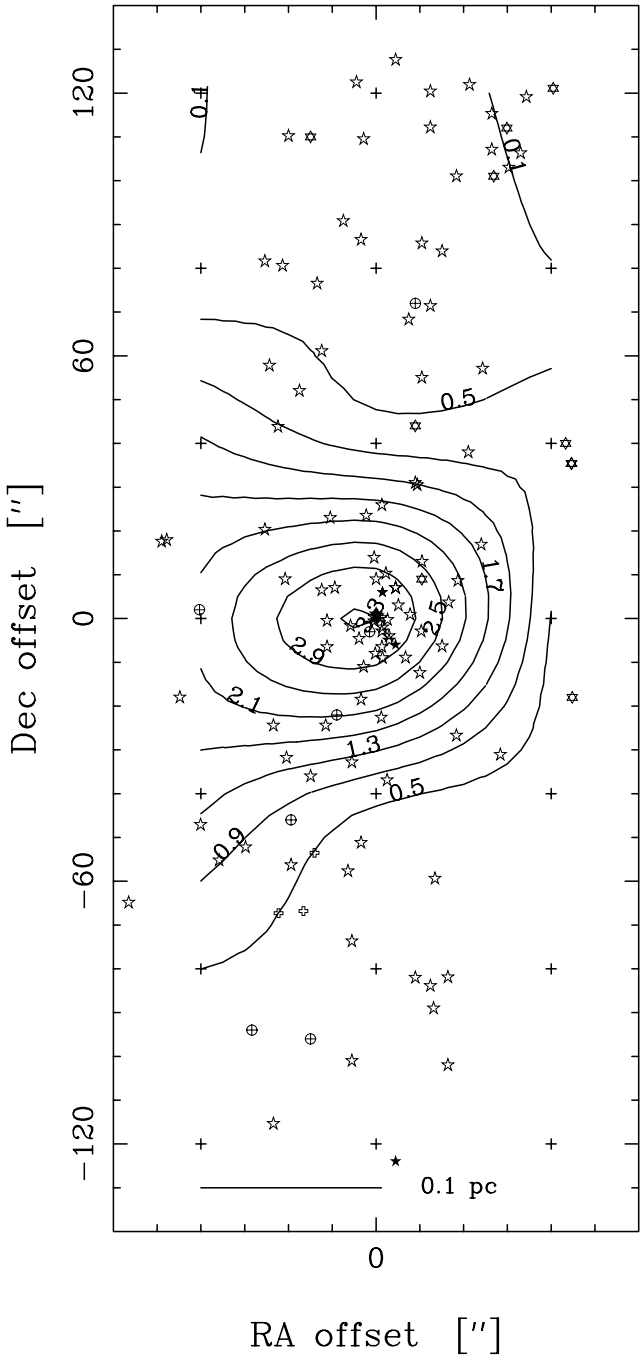

Fig. 1n. The SO/CS integrated intensity ratio in Orion A (outflow component included)

Table 3. Integrated intensity ratios (A–E) and estimated abundance ratios (F) at certain positions

Source	Offset ($''$,$''$)	Ratio A SO/^{34}SO	Ratio B CS/C^{34}S	Ratio C SO/CS	Ratio D ^{34}SO/C^{34}S	Ratio E Adopted	Ratio F [SO]/[CS]
DR 21(OH)	(−40,0)		8.2(0.3)	0.42(0.02)		0.16(0.01)[b]	0.6
DR 21(OH)	(0,−40)		6.3(0.1)	0.43(0.01)		0.12(0.00)[b]	0.5
DR 21(OH)	(0,−160)	24.3(5.0)	7.9(0.2)	0.27(0.02)	0.09(0.02)	0.09(0.02)[a]	0.4
DR 21(OH)	(0,0)	20.5(0.9)	6.7(0.1)	0.47(0.01)	0.15(0.01)	0.15(0.01)[a]	0.6
DR 21(OH)	(0,40)		7.4(0.3)	0.49(0.02)		0.17(0.01)[b]	0.7
DR 21(OH)	(40,0)		10.9(0.8)	0.27(0.02)		0.13(0.02)[b]	0.5
G 34.3+0.2	(−40,0)		5.2(0.4)	0.39(0.02)		0.09(0.01)[b]	0.4
G 34.3+0.2	(0,−40)		5.7(0.5)	0.33(0.02)		0.08(0.01)[b]	0.3
G 34.3+0.2	(0,0)	18.1(1.0)	4.8(0.1)	0.40(0.01)	0.11(0.01)	0.11(0.01)[a]	0.4
G 34.3+0.2	(0,40)		4.7(0.3)	0.38(0.03)		0.08(0.01)[b]	0.3
G 34.3+0.2	(40,0)		5.3(0.4)	0.51(0.04)		0.12(0.01)[b]	0.5
IRAS 21391+5802	(0,0)	20.6(4.9)	15.6(1.1)	0.41(0.02)	0.31(0.08)	0.31(0.08)[a]	1.3
Mon R2	(0,0)		7.7(0.3)	0.25(0.01)		0.09(0.00)[b]	0.4
Mon R2	(0,40)		9.7(0.6)	0.18(0.01)		0.08(0.01)[b]	0.3
NGC 1333	(0,0)		11.5(1.1)	0.23(0.01)		0.12(0.01)[b]	0.5
NGC 1333	(40,−40)	23.4(5.4)	17.2(5.8)	0.72(0.02)	0.53(0.21)	0.53(0.21)[a]	2.2
NGC 1333	(40,−160)	18.2(7.6)	9.6(0.9)	0.61(0.04)	0.32(0.14)	0.32(0.14)[a]	1.3
NGC 1333	(80,−40)	10.9(1.1)	8.1(0.7)	0.93(0.03)	0.70(0.09)	0.70(0.09)[a]	2.9
NGC 1333	(80,−80)	14.2(2.3)	12.5(2.9)	1.11(0.04)	0.97(0.28)	0.97(0.28)[a]	4.0
NGC 1333	(80,−120)	11.8(2.0)	5.9(0.4)	0.84(0.03)	0.42(0.08)	0.42(0.08)[a]	1.7
NGC 1333	(80,−160)	10.9(1.2)	11.2(0.8)	0.80(0.03)	0.83(0.11)	0.83(0.11)[a]	3.3
NGC 1333	(80,0)	14.2(2.1)	9.5(0.7)	0.78(0.02)	0.53(0.09)	0.53(0.09)[a]	2.2
NGC 1333	(80,40)	11.1(2.8)	22.0(7.7)	0.85(0.05)	1.68(0.72)	1.68(0.42)[c]	6.9
NGC 1333	(120,−200)	6.1(0.8)	8.6(0.9)	0.76(0.05)	1.08(0.17)	1.08(0.17)[a]	4.4
NGC 1333	(120,−40)	10.8(1.9)	13.4(2.4)	1.03(0.05)	1.27(0.31)	1.27(0.31)[a]	5.2
NGC 1333	(120,−80)	10.0(3.7)	14.6(3.8)	0.82(0.06)	1.19(0.54)	1.19(0.54)[a]	4.8
NGC 1333	(120,−120)	12.6(2.1)	7.6(1.0)	0.90(0.03)	0.54(0.11)	0.54(0.11)[a]	2.2
NGC 1333	(120,−160)	5.5(0.5)	6.6(0.8)	1.30(0.04)	1.56(0.23)	1.56(0.23)[a]	6.4
NGC 1333	(120,0)	11.8(3.4)	16.1(3.8)	0.72(0.05)	0.98(0.36)	0.98(0.36)[a]	4.0
NGC 1333	(120,40)		10.7(2.1)	0.66(0.06)		0.32(0.07)[b]	1.3
NGC 1333	(160,−120)	6.0(1.3)	16.6(5.9)	0.61(0.05)	1.69(0.70)	1.69(0.70)[a]	6.9
NGC 1333	(160,−160)	9.6(1.6)	7.8(1.1)	1.05(0.06)	0.85(0.18)	0.85(0.18)[a]	3.5
NGC 2023	(0,0)			0.22(0.03)		0.22(0.03)[d]	0.9
NGC 2024	(−40,0)		9.9(1.2)	0.23(0.02)		0.10(0.01)[b]	0.4
NGC 2024	(0,−40)	18.8(2.8)	8.3(0.4)	0.27(0.01)	0.12(0.02)	0.12(0.02)[a]	0.5
NGC 2024	(0,0)		7.2(0.2)	0.31(0.01)		0.10(0.00)[b]	0.4
NGC 2024	(0,40)	14.9(2.6)	7.7(0.4)	0.25(0.01)	0.13(0.02)	0.13(0.02)[a]	0.5
NGC 2024	(40,0)		6.0(0.6)	0.46(0.04)		0.13(0.01)[b]	0.5
NGC 2068	(0,0)		11.0(1.9)	0.25(0.03)		0.14(0.03)[b]	0.6
NGC 2068	(120,−80)	16.0(4.8)		1.26(0.26)		1.26(0.26)[d]	5.1
NGC 2071	(0,0)		5.9(0.3)	0.20(0.02)		0.05(0.01)[b]	0.2
NGC 2264IR	(−40,0)		10.6(0.6)	0.30(0.01)		0.14(0.01)[b]	0.6
NGC 2264IR	(0,−40)		8.3(0.4)	0.36(0.01)		0.14(0.01)[b]	0.6
NGC 2264IR	(0,0)	17.6(1.2)	9.8(0.3)	0.56(0.01)	0.31(0.02)	0.31(0.02)[a]	1.3
NGC 2264IR	(0,40)		6.8(0.4)	0.67(0.02)		0.21(0.02)[b]	0.8
NGC 2264IR	(40,0)		8.3(0.5)	0.59(0.02)		0.22(0.02)[b]	0.9
NGC 7538	(−40,0)		14.1(1.5)	0.32(0.02)		0.21(0.02)[b]	0.8
NGC 7538	(0,−40)	20.5(1.8)	8.2(0.3)	0.46(0.01)	0.19(0.02)	0.19(0.02)[a]	0.8
NGC 7538	(0,0)	18.5(2.2)	8.4(0.3)	0.28(0.00)	0.13(0.02)	0.13(0.02)[a]	0.5
NGC 7538	(0,40)		10.1(1.1)	0.51(0.05)		0.23(0.03)[b]	0.9
NGC 7538	(40,0)		5.6(0.3)	0.65(0.02)		0.17(0.01)[b]	0.7

a(b) denotes value(1σ error) where an error of (0.00) means 1σ error < 0.005 Ratio A: SO(3_2-2_1)/^{34}SO(3_2-2_1), Ratio B: CS$(2-1)$/C^{34}S$(2-1)$, Ratio C: SO(3_2-2_1)/CS$(2-1)$ Ratio D: ^{34}SO(3_2-2_1)/C^{34}S$(2-1)$, Ratio E: adopted SO/CS ratio, calculated for optically thin lines, T_{ex} = 20 K (see text). Explanations of the adopted SO/CS ratio: [a]: ^{34}SO(3_2-2_1)/C^{34}S$(2-1)$, [b]: SO(3_2-2_1)/(22×C^{34}S$(2-1)$), [c]: 22×^{34}SO(3_2-2_1)/CS$(2-1)$, [d]: SO(3_2-2_1)/CS$(2-1)$

Table 3. (continued)

Source	Offset ($''$,$''$)	Ratio A SO/^{34}SO	Ratio B CS/C^{34}S	Ratio C SO/CS	Ratio D ^{34}SO/C^{34}S	Ratio E Adopted	Ratio F [SO]/[CS]
OMC–2	(0,0)		14.8(1.3)	0.14(0.01)		0.09(0.01)[b]	0.4
OMC–3	(0,0)		10.7(1.0)	0.58(0.03)		0.28(0.02)[b]	1.1
Orion A	(−40,0)		6.4(0.3)	0.09(0.01)		0.03(0.00)[b]	0.1
Orion A	(0,−40)		10.1(0.6)	0.15(0.01)		0.07(0.01)[b]	0.3
Orion A	(0,−80)		5.0(0.2)	0.23(0.01)		0.05(0.00)[b]	0.2
Orion A	(0,0)		5.7(0.1)	0.11(0.01)		0.03(0.00)[b]	0.1
Orion A	(0,40)		7.4(0.4)	0.18(0.02)		0.05(0.01)[b]	0.2
Orion A	(40,0)		7.9(1.0)	0.32(0.02)		0.11(0.02)[b]	0.5
S 140	(−40,0)		8.8(0.6)	0.46(0.01)		0.18(0.01)[b]	0.7
S 140	(0,−40)		11.1(1.1)	0.27(0.01)		0.14(0.02)[b]	0.6
S 140	(0,0)	7.9(0.7)	8.9(0.4)	0.40(0.00)	0.45(0.04)	0.45(0.04)*a*	1.9
S 140	(0,40)		8.5(0.5)	0.44(0.01)		0.17(0.01)[b]	0.7
S 140	(40,0)		7.4(0.5)	0.30(0.01)		0.10(0.01)[b]	0.4
W3(IRS4)	(−40,−40)		10.8(0.6)	0.31(0.02)		0.15(0.01)[b]	0.6
W3(IRS4)	(−40,0)		8.0(0.7)	0.43(0.02)		0.16(0.02)[b]	0.6
W3(IRS4)	(−40,40)		17.8(5.1)	0.35(0.03)		0.29(0.09)[b]	1.1
W3(IRS4)	(0,−40)	19.4(2.3)	7.3(0.2)	0.34(0.01)	0.13(0.02)	0.13(0.02)[a]	0.5
W3(IRS4)	(0,0)		6.6(0.1)	0.29(0.00)		0.09(0.00)[b]	0.4
W3(IRS4)	(0,40)		8.2(0.9)	0.23(0.02)		0.08(0.01)[b]	0.3
W3(IRS4)	(40,−40)		11.6(0.8)	0.45(0.01)		0.24(0.02)[b]	0.9
W3(IRS4)	(40,0)		12.8(1.0)	0.36(0.01)		0.21(0.02)[b]	0.8
W3(IRS4)	(40,40)		20.3(5.1)	0.20(0.03)		0.18(0.05)[b]	0.7
W3(OH)	(−40,0)		7.1(0.4)	0.46(0.02)		0.15(0.01)[b]	0.6
W3(OH)	(0,−40)		15.0(1.4)	0.31(0.01)		0.21(0.02)[b]	0.8
W3(OH)	(0,0)	23.4(2.4)	7.4(0.2)	0.49(0.01)	0.15(0.02)	0.15(0.02)*a*	0.6
W3(OH)	(0,40)		12.8(1.1)	0.23(0.01)		0.13(0.01)[b]	0.5
W3(OH)	(40,0)		11.0(0.6)	0.30(0.02)		0.15(0.01)[b]	0.6
W 49N	(−40,0)		6.1(0.2)	0.38(0.01)		0.10(0.00)[b]	0.4
W 49N	(0,−40)		9.3(0.5)	0.41(0.02)		0.17(0.01)[b]	0.7
W 49N	(0,0)	10.8(0.2)	7.6(0.1)	0.76(0.00)	0.54(0.01)	0.54(0.01)[a]	2.2
W 49N	(0,40)		6.7(0.2)	0.34(0.01)		0.10(0.01)[b]	0.4
W 49N	(40,0)		7.7(0.2)	0.43(0.01)		0.15(0.01)[b]	0.6
W 51N	(−40,−40)		6.5(0.1)	0.36(0.01)		0.11(0.00)[b]	0.4
W 51N	(−40,0)		7.0(0.2)	0.38(0.01)		0.12(0.00)[b]	0.5
W 51N	(−40,40)		12.0(0.6)	0.28(0.01)		0.15(0.01)[b]	0.6
W 51N	(0,−40)		6.1(0.1)	0.27(0.01)		0.08(0.00)[b]	0.3
W 51N	(0,0)	20.2(1.2)	6.1(0.1)	0.36(0.01)	0.11(0.01)	0.11(0.01)[a]	0.4
W 51N	(0,40)		9.5(0.5)	0.23(0.01)		0.10(0.01)[b]	0.4
W 51N	(40,−40)	17.4(0.6)	4.9(0.1)	0.37(0.00)	0.10(0.00)	0.10(0.00)[a]	0.4
W 51N	(40,0)		5.7(0.1)	0.33(0.01)		0.09(0.00)[b]	0.4
W 51N	(40,40)		7.5(0.4)	0.27(0.01)		0.09(0.01)[b]	0.4

a(b) denotes value(1σ error) where an error of (0.00) means 1σ error < 0.005 Ratio A: SO($3_2 - 2_1$)/^{34}SO($3_2 - 2_1$), Ratio B: CS($2 - 1$)/C^{34}S($2 - 1$), Ratio C: SO($3_2 - 2_1$)/CS($2 - 1$) Ratio D: ^{34}SO($3_2 - 2_1$)/C^{34}S($2 - 1$), Ratio E: adopted SO/CS ratio, calculated for optically thin lines, T_{ex} = 20 K (see text). Explanations of the adopted SO/CS ratio: [a]: ^{34}SO($3_2 - 2_1$)/C^{34}S($2 - 1$), [b]: SO($3_2 - 2_1$)/(22×C^{34}S($2 - 1$)), [c]: 22×^{34}SO($3_2 - 2_1$)/CS($2 - 1$), [d]: SO($3_2 - 2_1$)/CS($2 - 1$)

we may now proceed to calculate the ratio of the total SO and CS column densities. Here the $g_u = 2J_u + 1$ is the statistical weight of the upper state whose energy is E_u and whose total angular momentum quantum number is J, k is the Boltzmann constant, T is the population distribution ("rotation") temperature and $Q(T)$ is the molecular partition function evaluated at temperature T. The partition function for a linear molecule may (for not too low T) be approximated by

$$Q(T) = \sigma \frac{kT}{hB}, \tag{6}$$

where h is Planck's constant and B is the molecular rotation constant. Here $\sigma = 1$ for CS and $\sigma \approx 3$ for SO [accounting

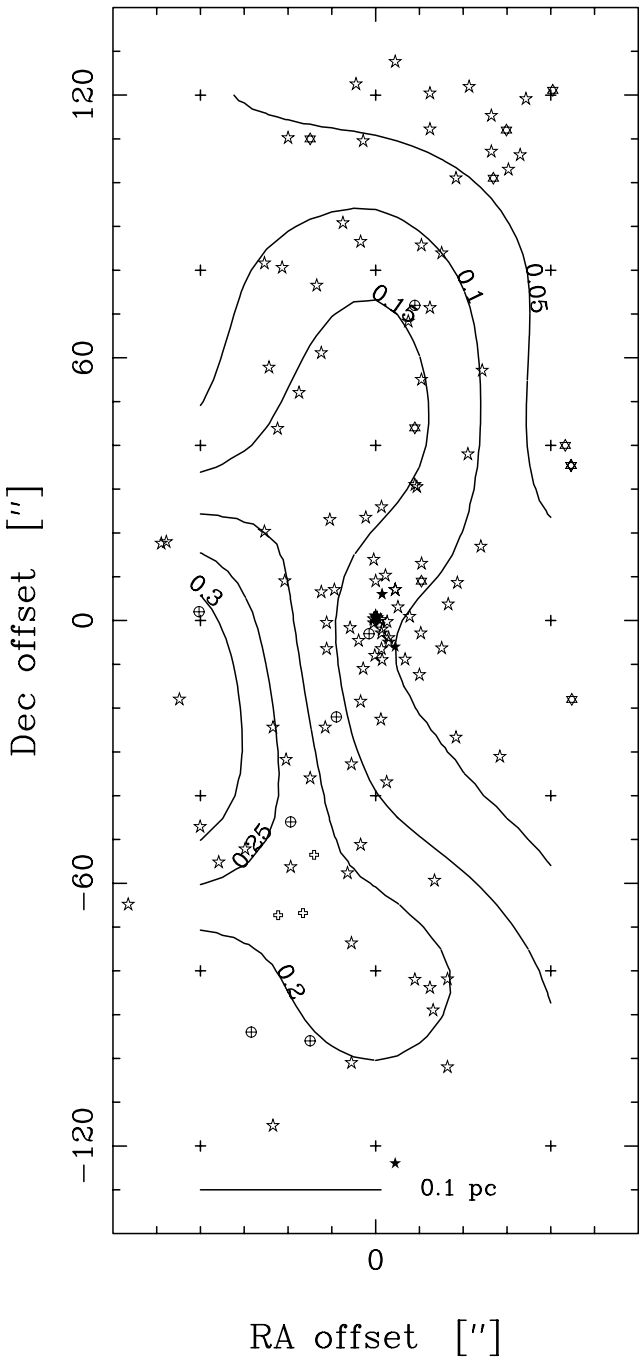

Fig. 1o. The SO/CS integrated intensity ratio in Orion A, with outflow and hot core components removed

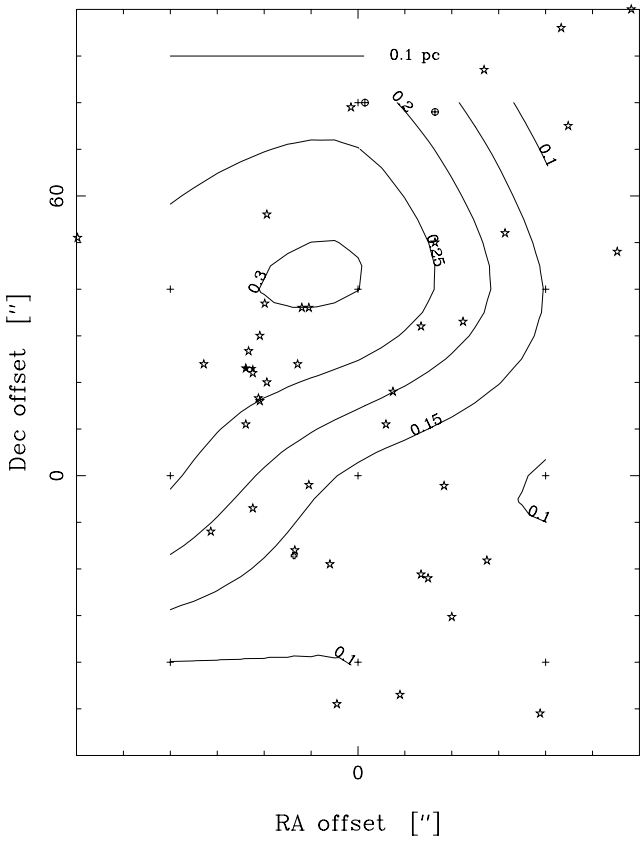

Fig. 1p. The SO/CS integrated intensity ratio in OMC–2

for the threefold multiplicity of its $^3\Sigma$ ground state, cf. Turner (1991)]. Using the approximate partition function, Eq. (6), together with Eqs. (4) and (5), we finally arrive at the following useful measure of the SO to CS abundance ratio,

$$\frac{N(\mathrm{SO})}{N(\mathrm{CS})} \approx 3.6 \times \frac{T_{\mathrm{SO}}}{T_{\mathrm{CS}}} \times \exp\left(\frac{E_{\mathrm{SO}}}{kT_{\mathrm{SO}}} - \frac{E_{\mathrm{CS}}}{kT_{\mathrm{CS}}}\right) \times \frac{I_{\mathrm{SO}}}{I_{\mathrm{CS}}}.$$

If we assume the same excitation temperature, T, for both species this relation simplifies to

$$\frac{N(\mathrm{SO})}{N(\mathrm{CS})} \approx 3.6 \times \exp(2.2/T) \times \frac{I_{\mathrm{SO}}}{I_{\mathrm{CS}}}, \quad (7)$$

where the proper molecular parameters have been entered. We note that according to Eq. (7) the conversion factor determining $N(\mathrm{SO})/N(\mathrm{CS})$ from $I_{\mathrm{SO}}/I_{\mathrm{CS}}$ only varies from 4.5 to 3.9 if the common excitation temperature changes from 10 K to 30 K. The SO/CS abundance ratios entered in the last column of Table 3 are calculated for $T = 20$ K. We will now proceed to motivate our simplified analytical approach by some exploratory Monte Carlo simulations.

2.4. Monte Carlo simulations

In order to verify that the above estimate of the SO/CS abundance ratio is not severely affected by non-LTE excitation effects we have performed Monte Carlo simulations (cf. Bernes 1979) using a spherical model cloud of radius 10^{18} cm (divided into 19 concentrical shells of equal volume) exposed to the cosmic background radiation (T=2.73 K). The abundance, H_2 density, and kinetic temperature, T_{k}, were all kept constant throughout the cloud. For CS and SO we included all levels with excitation energies below 400 K. Collisional rate coefficients for SO-H_2 were taken from Green (1994) and for CS-H_2 we used those reported by Turner et al. (1992). The modelled line intensities were obtained by numerically integrating the intensity along rays at different offsets from the model cloud center and adding

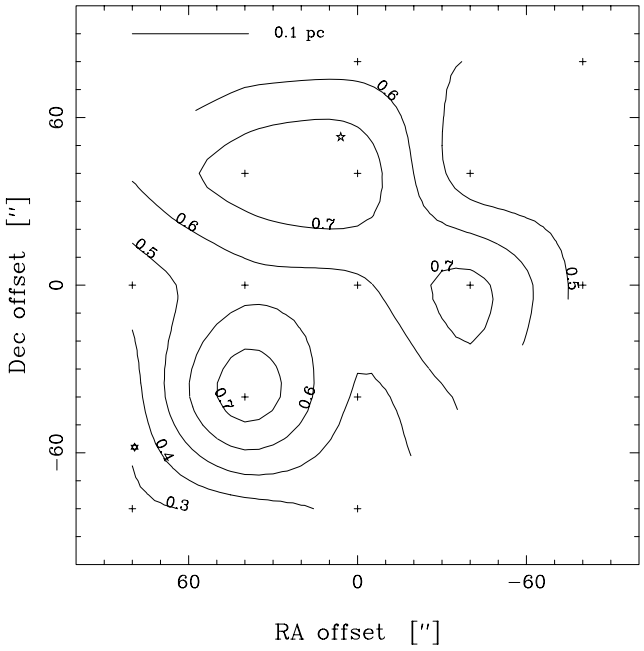

Fig. 1q. The SO/CS integrated intensity ratio in OMC–3

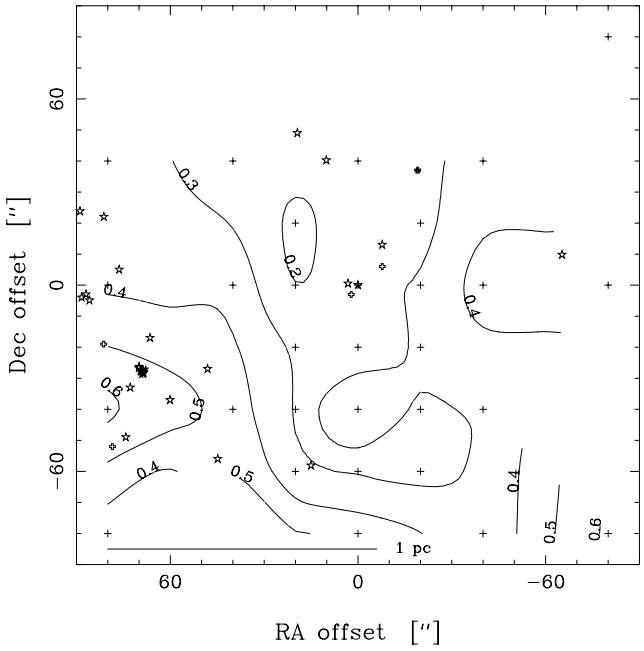

Fig. 1s. The SO/CS integrated intensity ratio in W3(IRS4)

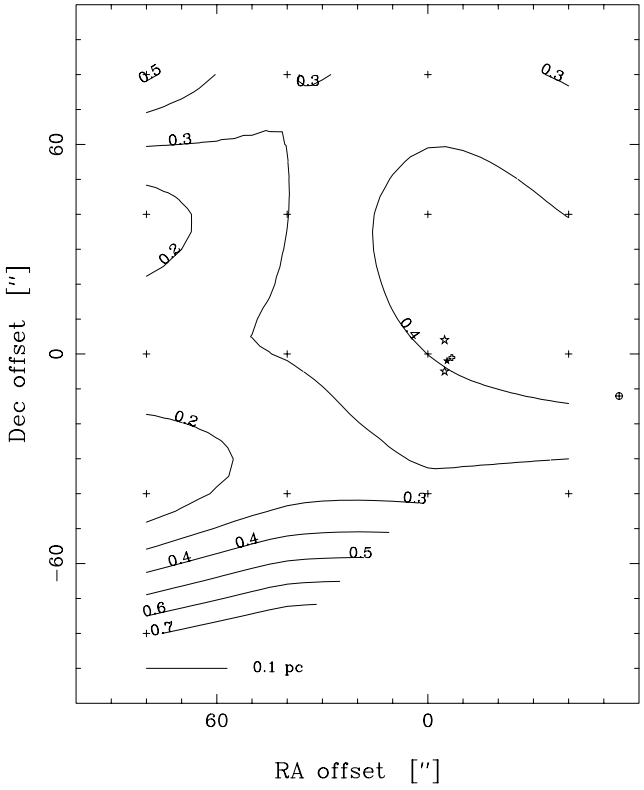

Fig. 1r. The SO/CS integrated intensity ratio in S 140

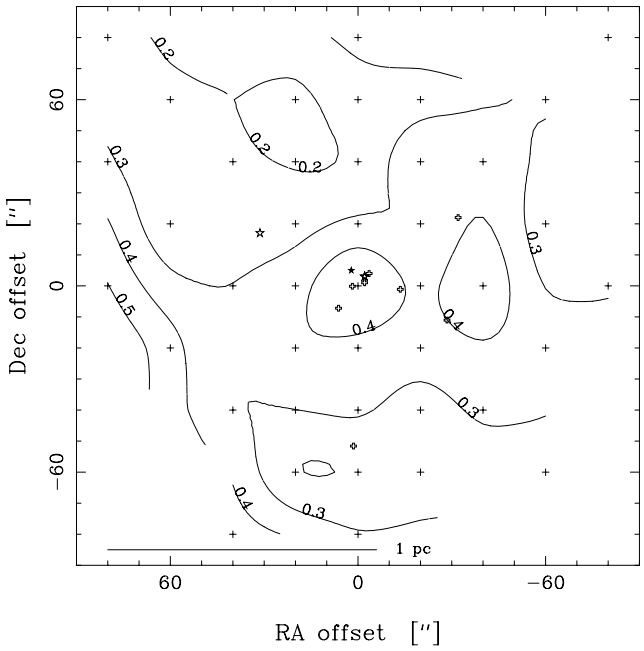

Fig. 1t. The SO/CS integrated intensity ratio in W3(OH)

together the contributions from each ray with a proper weight corresponding to a gaussian beam of width 39″. The model cloud was assumed to be at a distance of 1 kpc.

We have performed Monte Carlo simulations for CS and SO at four different abundances in the range $10^{-10} - 4 \times 10^{-9}$ at several H_2 densites in the range $10^{2.75} - 10^8\,\mathrm{cm}^{-3}$. The kinetic temperature was 30 K in all simulations. The results are presented in Fig. 3, where the SO$(3_2 - 2_1)$/CS$(2-1)$ integrated intensity ratio is plotted as a function of molecular column density through the center of the model cloud. The displayed intensity ratio reflects the case when the molecular column density is the same for both species. The CS and SO lines start to become optically thick at column densities $N[\mathrm{CS, SO}] = 10^{14} - 10^{15}\,\mathrm{cm}^{-2}$. At lower column densites (and low H_2 densities since the cloud size is constant) the excitation is highly subthermal, and at high column densities (also high H_2 densities) the ratio approaches

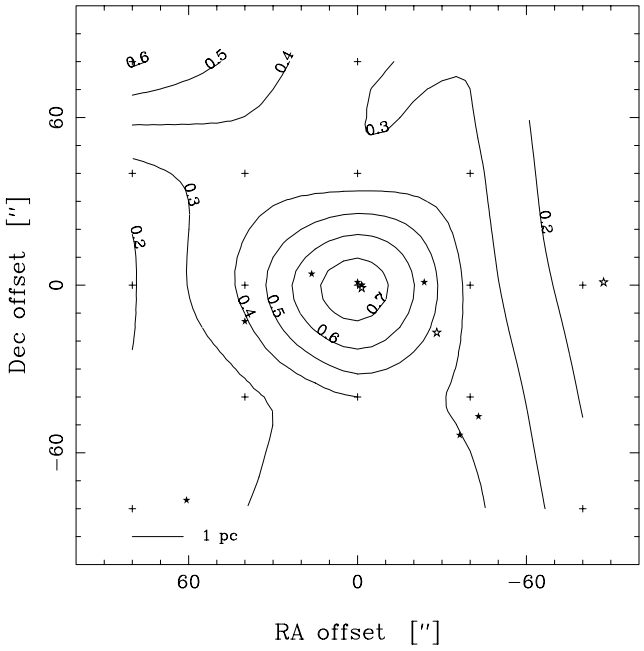

Fig. 1u. The SO/CS integrated intensity ratio in W 49N

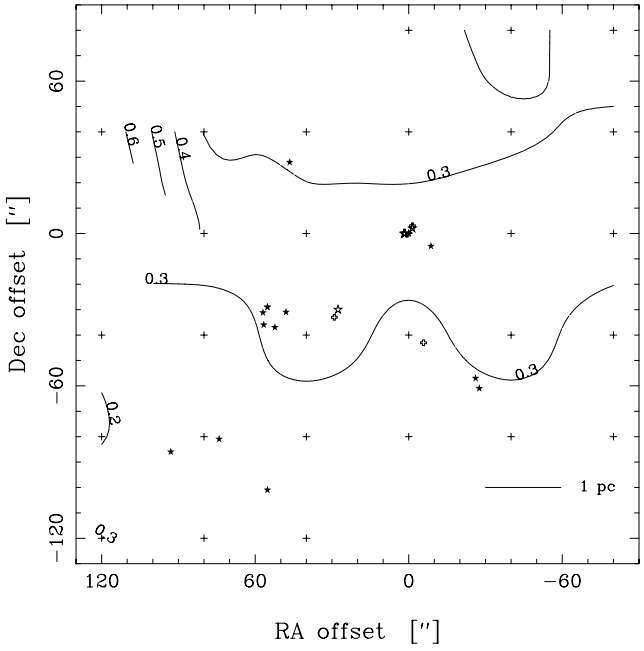

Fig. 1v. The SO/CS integrated intensity ratio in W 51N

1 when both lines are very optically thick. The reason why the limit ratio is slightly below 1 is that the optical depth broadening is somewhat larger for the CS line as compared to the SO line. Judging from the Monte Carlo results shown in Fig. 3 we find that the variation of the SO/CS integrated intensity ratio is fairly small for a large range of H_2 densities and abundances, and that the variations that do occur are mainly due to optical depth effects. Here the lowest abundance (10^{-10}) should be representative of ^{34}SO/C^{34}S data. We conclude that the simplified analysis presented in Sect. 2.3 is sufficiently accurate for our purposes.

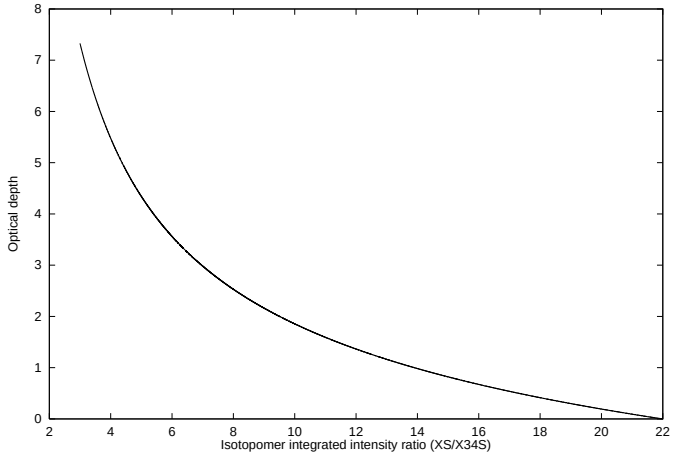

Fig. 2. SO or CS main line optical depth as function of main line to isotopomer ratio (assuming the same $T_{\rm ex}$ for both isotopomers and a ^{32}S/^{34}S ratio of 22)

3. Results of astrochemical simulations

We have performed gas–phase chemical simulations using the entire UMIST RATE95 reaction rate database (Millar et al. 1997). Some relevant parameters have been varied in one dimension at a time [for a multi–dimensional variation see Nilsson (1999)]. The initial elemental abundances were adopted from Bergin et al. (1997), but adding helium and chlorine (see Table 4). The chemical model consists of an average central cloud position characterized by the input parameters. We have solved the coupled ordinary differential equations using the Gear method (Gear 1971a, 1971b; Hindmarsh 1972a, 1972b; Hindmarsh & Gear 1974). Unless otherwise stated the visual extinction has been set to 25 mag, the cloud temperature to T = 20 K, and the cloud density to $n(\mathrm{H_2}) = 10^5\,\mathrm{cm}^{-3}$. We have assumed a standard cosmic ray ionization rate $\zeta_0 = 1.3 \times 10^{-17}$ s^{-1} and a UV–light flux of 1 Habing. Variations in the cosmic–ray ionization rate are used here to model, in an approximate manner, the influence of X–ray irradiation on the chemical evolution. For the adopted visual extinction the influences of the UV–light are negligible. The simulation results are presented in Figs. 4–21.

The reason why we are studying influences of X–rays in the present context is the fact that young stellar objects (YSO) have been observed to be strong X-ray emitters (e.g. Casanova et al. 1995). In fact, already Krolik & Kallman (1983) have demonstrated that the X–ray sources observed near the core of the Orion molecular cloud would be sufficient to supply the ionization needed to drive the ion–molecule chemistry, even if cosmic ray ionization were not available. The reason is that the secondary ionization caused by Auger and photoelectrons here dominates over the direct X–ray photoionization by more than an order of magnitude [see Krolik & Kallman (1983), and also the discussion by Casanova et al. (1995)]. These authors also

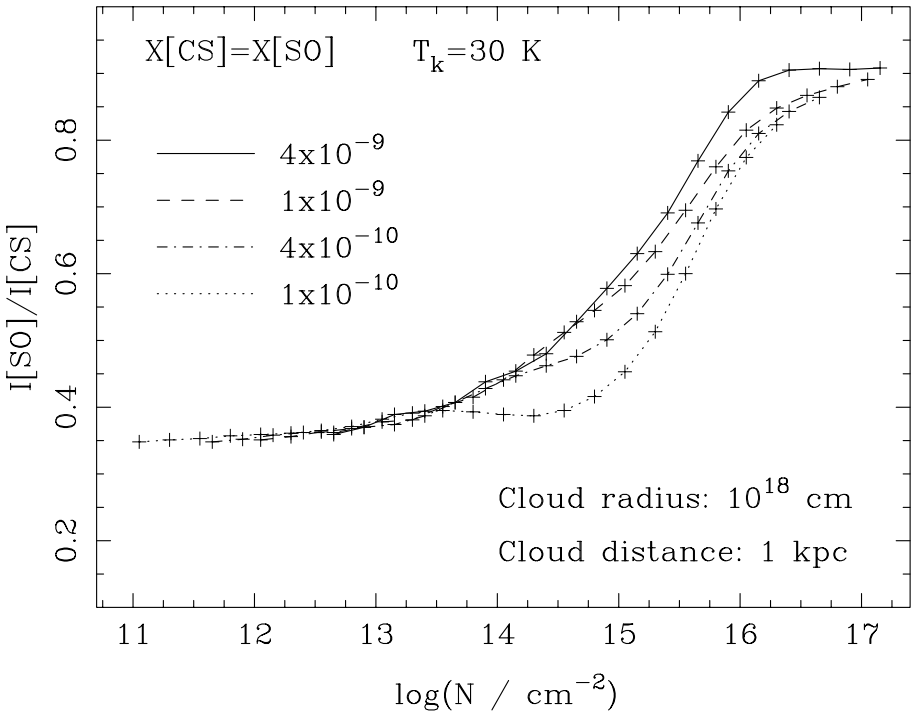

Fig. 3. The SO(3_2-2_1)/CS($2-1$) integrated intensity ratio as function of molecular column density ($N_{\rm CS} = N_{\rm SO}$) for a Monte Carlo model cloud of radius 10^{18} cm.

Table 4. Initial fractional abundances[a]

Element	Abundance (relative H_2)
C^+	1.46×10^{-4}
N	4.28×10^{-5}
O	3.52×10^{-4}
S^+	4.00×10^{-8}
Si^+	4.00×10^{-8}
Mg^+	6.00×10^{-9}
Fe^+	6.00×10^{-9}
Na^+	4.00×10^{-9}
P^+	6.00×10^{-9}
He	1.40×10^{-1}
Cl	8.00×10^{-9}

[a] From Bergin et al. (1997) but adding He and Cl

argue that in localized regions around the X–ray emitting YSO's the ionization rate would become considerably enhanced. Already the chemical modelling by Krolik & Kallman (1983) demonstrated an accelerated formation of molecules as the ionization rate is increasing. However, for very high ionization rates H_2 and most other molecules would be destroyed (cf. Lepp & Dalgarno 1996).

3.1. Temporal evolution

As mentioned in the introduction the original idea behind this project was to find out if the SO/CS abundance ratio could probe the temporal evolution of a molecular cloud. In Fig. 4 we display the abundance variations as a function of time for a number of species relevant to the present project. The time development is just as expected from our earlier discussion (in the introduction) of the dominant formation and destruction mechanisms. While CS and CO reach a high abundance at "early times" the SO and O_2 abundances can rise to observable abundances only when their efficient destruction in reactions with free C (reactions 2) is diminished. This happens at "late times" when most C has been locked up in CO. In Fig. 4 we also see that the CS abundance decreases by an order of magnitude at late times. The main reason is efficient CS destruction via

$$\mathrm{CS} + \mathrm{O} \rightarrow \mathrm{CO} + \mathrm{S}$$

since the amount of free O remains high. For the adopted initial elemental abundances (Table 4) the late time fractional abundances w.r.t. H_2 of SO, CS, O_2, and CO become $1.6 \times 10^{-8}, 2.7 \times 10^{-9}, 5.7 \times 10^{-5}$, and 1.4×10^{-4}, respectively. We do indeed confirm the temporal development present in earlier studies including those by Bergin et al. (1995) and Lee et al. (1996). Here the initial elemental abundances have been chosen such that the model will match the observed abundances of CO, CS, SO etc, "as well as possible". A striking consequence of this forced match between modelling and observations is a predicted O_2 abundance of 6×10^{-5} ([O_2]/[CO] = 0.4), which is more than an order of magnitude above the lowest reported observational limits from ground based (Maréchal et al. 1997a); balloon–borne PIROG 8 (Olofsson et al. 1998); and satellite–borne SWAS (Melnick et al. 1999) observations. We here just note that a "cure" to this problem would be to "adopt" a lower O/C abundance ratio (cf. Figs. 6 and 9), and will return to this question in the comparison of our SO/CS observational data with models. The variations of the O_2/SO abundance ratio vs time, as calculated from the model results in Fig. 4, are shown in Fig. 7. In Figs. 5 and 8 we show the time development of the SO/CS and O_2/CO abundance ratios, respectively.

3.2. O/C$^+$ variation

The "standard" [C]/[O] interstellar abundance ratio value is 0.4. We have performed calculations to study the sensitivity of the SO/CS and O_2/CO abundance ratios to variations in the O/C$^+$ initial abundance ratio. The resulting SO/CS and O_2/CO abundance ratios are shown in Figs. 6 and 9, respectively. It is indeed very obvious that these ratios are very sensitive to the initial O/C$^+$ abundance ratio, especially in the range 1–2. High SO and O_2 abundances can only develop if O/C$^+ > 1.5$. A decrease below this value rapidly leads to very low SO and O_2 abundances. In case of SO this behaviour has been discussed at some length by Bergin et al. (1997) (cf. their Fig. 6).

3.3. Density variations

We also ran simulations for varying H_2 number density. The results are displayed in Figs. 10 and 13. The final SO/CS abundance ratio is increased by an order of magnitude as the cloud density (H_2 number density) is increased from 10^3 to 10^6 cm^{-3}, whereas the O_2/CO ratio is not sensitive to the density. We also clearly see a considerably faster chemical evolution as the density increases, which indeed is expected as a result of increasing collision rates between the reaction partners.

3.4. Variations of the (X–ray) ionization level

To study the influence of variations of the X–ray radiation we defined a scaling factor $F = \zeta/\zeta_0$, where ζ is the actual ionization rate and ζ_0 is the standard cosmic ray ionization rate. An increased cosmic ray ionization rate will accomplish the same thing as would an X–ray source, as explained at the beginning of this section.

Figs. 11 and 14 demonstrate the dramatic change of the time dependence resulting from variations of the ionization level. The chemical evolution becomes much faster as the increasing ionization produces a higher H_3^+ abundance (Fig. 16) which leads to more OH (Fig. 19) and a subsequent formation of more SO and O_2 (reactions 1). We note that the abundances of H_3^+, OH, C$^+$ and C *increase* about linearly with the scaling factor F, and also that the time scale *decreases* strongly with increasing F. We also note that the late time abundances of SO and O_2 decrease with increasing ionization level, however much less pronounced for O_2. Such an SO abundance decrease at late times is readily explained by the loss reactions, since the increased ionization level also strongly influences the temporal evolution as well as the late time abundances of C, C$^+$, and CS (Figs. 17, 20, and 18, respectively). The influence of an increased ionization on the H_2O concentration is shown in Fig. 21. An increased ionization level leads to a higher abundance of H_2O as well as a faster chemistry. Again this is explainable in terms of an increased production of H_3^+ with subsequent formation of H_3O^+, from which H_2O as well as OH are formed via dissociative recombination with electrons. However, this branching ratio still is somewhat uncertain (cf. Herbst & Lee 1997).

Similar results have been obtained by Farquhar et al. (1994). These authors also note, in accordance with our findings, that the SO/CS abundance ratio may be a useful diagnostic of chemical evolution ("cloud age"). However, this clean picture may become rather deteriorated by the very sensitive dependence of the SO abundance upon the initial O/C$^+$ ratio.

3.5. Sulphur variations

Figs. 12 and 15 show that the SO/CS and O_2/CO abundance ratios do not depend severely on the initial sulphur content (even though the SO and CS abundances themselves vary rather linearly with the initial S abundance). Only if the S content is increased by a factor of 1000 does the O_2/CO abundance ratios decrease by a visible amount (a factor of ~ 2).

4. Discussion

A lot of SO/CS observations have been presented as well as some exploratory chemical modelling. Large variations in the SO/CS abundance ratio can be explained by differences in "chemical age", density, initial oxygen abundance, as well as varying ionization levels caused by cosmic ray flux or X–ray sources.

4.1. The observed variations of the SO/CS abundance ratio in the light of chemical modelling

As evident from our ratio maps (Figs. 1a–1v) and the more accurate determinations from ^{34}SO and C^{34}S observations (Table 3) the SO/CS abundance ratio exhibits pronounced variations, well outside the relevant error bars, *between* the nineteen cloud cores of our sample as well as *within* some of the clouds. This is indeed neither unexpected nor astonishing in the light of the exploratory chemical modelling presented in Sect. 3.

We propose that *the main cause of the variation* of the SO/CS abundance ratio *between clouds is the very high sensitivity to a variation of the initial* O/C$^+$ *elemental abundance ratio* (see Fig. 6). Relatively small variations of the elemental abundances/depletions of oxygen and carbon among the clouds would be required. Some influences of variations of the cosmic ray and/or X–ray flux may also be present, since the propagation of cosmic ray particles would be sensitive to e.g. variations of the Galactic magnetic field, while the X–rays originate in young stellar objects. Likewise, some influences of cloud age and more or less rapid chemical evolution due to somewhat different average cloud densities cannot be excluded. Moreover, variations of the UV light flux as well as lower visual extinction (than the 25 mag assumed in the modelling) may be important in lower density clouds (cf. Nilsson 1999). Since the abundances of SO and CS are almost linearly dependent upon the available amount of free sulphur, the SO/CS abundance ratio is essentially insensitive to the initial S abundance (as is apparent from Fig. 12). We will, however, return to all these questions in a subsequent Paper III (Olofsson et al., in prep.), where the very abundances of SO and CS, as well as the H_2 cloud and column densities, will be mapped across the clouds in the present sample.

We now turn to a general discussion of the observed large variations of the SO/CS abundance ratios within some clouds and the apparent lack of such variations within other clouds. It is again obvious from the chemical modelling results (Fig. 6) that relatively small variations of the initial oxygen and carbon abundances *could* cause large changes of the SO/CS ratio, but such local variations of the gas–phase elemental abundances may be less likely. They could though originate from different local depletions onto dust grains. Instead we propose that *where large local variations of* [SO]/[CS] *are observed this is more likely a consequence of the combined effects of density changes* (Fig. 10) *and local variations of the cosmic ray and X–ray ionization levels* (Fig. 11). *In all these cases the local chemical evolution is accelerated, resulting in a change of the time needed to reach a chemical steady state* and a large SO abundance. In this respect we may say that the SO/CS abundance ratio is a diagnostic of the "cloud age". We here also should note that an increasing local cosmic ray or X–ray ionization level leads to a somewhat reduced late time SO/CS abundance ratio, while, on the contrary, a density increase raises this ratio (cf. Figs. 11 and 10). Furthermore, since the propagation of (charged) cosmic ray particles would be sensitive to magnetic fields, we may indeed expect some local variations of the ionization in denser regions, where the magnetic field strength also is expected to increase due to "flux freezing". Large local increases of the X–ray ionization would be expected near YSO's, as has been so clearly demonstrated for the ρ Oph molecular cloud by Casanova et al. (1995).

In this rather pronounced framework of expectations *the apparent lack of SO/CS variations in many sources may be more surprising than our discovery of large variations within a few sources*. However, to some extent this may be an effect of spatial resolution, since large variations have been seen only in nearby clouds (cf. Table 5).

We have until now avoided a comparison of the chemical evolution time scale with other relevant time scales. One such time scale is the free–fall time – the characteristic collapse time of a pressure free gravitationally unstable gas core – which has been estimated to be $t_{\rm ff} \approx 4 \times 10^5/\sqrt{n/10^4}$ yr, where n is the H_2 volume density (particles per cm^3) (Spitzer 1978). We note that the free–fall time scale is of the same order of magnitude as the time needed to reach late time chemical equilibrium. Another time scale of concern in connection with chemical modelling is that relevant for molecular depletion onto cold dust grains. This molecular sticking time scale has been estimated to be $t_{\rm st} = 10^5\sqrt{m}/(y_{\rm s}n/10^4)$ yr, where m is the mass (in amu) of the molecule in question, $y_{\rm s}$ is the sticking efficiency and n is the H_2 volume density (cf. Williams 1993; Dzegilenko & Herbst 1995). The sticking efficiency is believed to fall in the range $y_{\rm s} = 0.1 - 1.0$, so that for SO and CS the "sticking time" becomes $t_{\rm st} = (7 - 70) \times 10^5/(n/10^4)$ yr, which is also of the same order of magnitude as the time required to approach ("late time") chemical equlibrium and hence could strongly influence the late time chemical abundances. However, since interstellar molecules are observed at abundance levels close to those predicted by pure gas phase models (without sticking), it appears that efficient desorption mechanisms must also exist. But their efficiency is rather uncertain, as are the sticking efficiencies of the various molecules (cf. Williams 1993; Bergin et al. 1995; Dzegilenko & Herbst 1995).

In our astrochemistry calculations we have not included molecular depletion onto/desorption from grain surfaces. In their extensive chemical modelling efforts Bergin et al. (1995) also investigated such processes. They suggest that if the interstellar grains have an outer layer of CO ice then the binding energies to the grain mantle may be considerably lower than commonly assumed for many species, and a significant amount of the molecules will remain in gas phase.

Table 5. O_2 late time abundance predictions, maximum values, resulting from [SO]/[CS] maximum

Source	Dist. (kpc)	[SO]/[CS] range[a]	[O]/[C$^+$] required[b]	[O_2]/[CO] predicted[c]
W3(IRS4)	2.4	0.3–1.1	1.6	0.1
W3(OH)	2.4	0.5–0.8	1.5	0.1
NGC 1333	0.35	0.5–6.9	2.5	0.4
Orion A	0.5	0.1–0.5	1.4	0.1
OMC–2	0.5	0.4	1.4	0.1
OMC–3	0.5	1.1	1.6	0.1
NGC 2023	0.4	0.9	1.5	0.1
NGC 2024	0.4	0.4–0.5	1.4	0.1
NGC 2068	0.4	0.6–5[d]	2.3	0.3
NGC 2071	0.4	0.2–7[e]	2.5	0.4
Mon R2	1.0	0.3–0.4	1.4	0.1
NGC 2264IR	0.9	0.6–1.3	1.6	0.1
G 34.3+0.2	3.7	0.3–0.5	1.4	0.1
W 49N	11.4	0.4–2.2[f]	1.8	0.2
W 51N	7.0	0.3–0.6	1.5	0.1
DR 21(OH)	3.0	0.4–0.7	1.5	0.1
IRAS 21391	0.8	1.3	1.6	0.1
S 140	0.9	0.4–1.9	1.7	0.2
NGC 7538	2.8	0.5–0.9	1.5	0.1
ρ Oph A,B	0.2	4[g]	2.2	0.3
Sgr B2(NW)	8.5	2.0[h]	1.8	0.2
TMC–1	0.1	0.3–1.3[i]	1.6	0.1
L 134N	0.2	1.7–6.7[j]	2.5	0.4
M 17	2.2	0.1–0.2[k]	1.3	0.05

[a] The adopted ratios of Table 3, if not otherwise stated
[b] Initial [O]/[C$^+$] required to get the observed [SO]/[CS] at late times for the highest observed [SO]/[CS], cf. Figs. 5 and 22, for $n[H_2] = 10^5$ cm^{-3}
[c] Maximum value at late times, for the [O]/[C$^+$] value in previous column, [O_2]/[H_2] is 10^{-4} times lower
[d] maximum value using SO($3_2 - 2_1$)/(22×C^{34}S($2 - 1$))
[e] maximum value from map using SO($3_2 - 2_1$)/CS($2 - 1$)
[f] possible influence of unresolved outflow, see text
[g] Using the SO data of Gottlieb et al. (1978), and CS data from Liseau et al. (1995), and unpublished SEST data
[h] N(SO)/(22×N(C^{34}S)) for the NW position of Nummelin et al. (2000)
[i] N(SO)/(22×N(C^{34}S)) for $(\Delta\alpha, \Delta\delta)$ = (0′,0′) and $(-3\farcm11, 5\farcm23)$, Pratap et al. (1997)
[j] Swade (1989a, 1989b)
[k] Bergin et al. (1997)

Therefore we have to stress that our exploratory chemical modelling (assuming no net adsorption onto grain surfaces) is indeed just a first step in considering what may cause variations in the SO/CS abundance ratio.

4.1.1. NGC 1333

The NGC 1333 molecular cloud, at a distance of only 350 pc, is the most nearby source in our sample. It is also unique in that the SO/CS abundance ratio rises from very low values near the driving source SVS 13 of a prominent outflow (Liseau et al. 1988) to very high values along an extended north–south elongated ridge at the end of the outflow. We have here mapped the variations of the SO/CS abundance ratio by means of the optically thin ^{34}SO(3_2-2_1) and C^{34}S($2-1$) transitions. The SO/CS abundance ratio is estimated to be as low as 0.5 near SVS 13, which is the (0,0) offset position in our maps (Figs. 1d–1e). In the north–south elongated ridge region the SO/CS abundance ratio falls in the range 2–7, with the highest ratio near the far infrared source IRAS 4 which is located about $200''$ from SVS 13. It is instructive to point out, when comparing to more distant sources, that if NGC 1333 would have been located at a distance further away than about 2–3 kpc it had not been possible to clearly discern the large variations with our $40''$ beam.

The same elongated ridge of gas is apparent in the ^{13}CO and C^{18}O 1–0 and 2–1 observations by Warin et al. (1996). These authors argue that this is a compressed "shell" of gas formed as the winds/outflows from SVS 13 (dynamical age $\sim 10^4$ yr) and several other nearby sources have swept up the material in the parent molecular cloud. The cloud density in this north–south elongated ridge was estimated to vary from 3×10^3 to 5×10^4 cm^{-3} and the H_2 column density is $(2-3)\times10^{22}$ cm^{-2}, corresponding to a visual extinction A_V, from the cloud core to the surface, of 11–16 mag (Bohlin et al. 1978). From their follow–up CS(2–1, 3–2, 5–4) mapping study of the NGC 1333 region Langer et al. (1996) derive an average density of 2×10^5 cm^{-3} in the compressed ridge. Warin et al. (1996) identified several massive ($\sim$ 20–40 M$_\odot$) condensations in the compressed shell, which were proposed to be potential sites for the formation of the next generation of stars. While the average temperature in the region is below 20 K, the temperature rises to 33–42 K in the cluster of 18–46 L$_\odot$ IRAS sources which is contained in the molecular cloud ridge (Jennings et al. 1987).

The extensive molecular line observations of one of these sources, IRAS 4, by Blake et al. (1995), have revealed a very dense (2×10^6 cm^{-3}) core at a kinetic temperature in the range 20–40 K. A young (dynamical age of a few thousand years) outflow also originates in this region.

This information about the physical conditions in the NGC 1333 core regions may clarify the large SO/CS abundance ratio variations across this region. According to our chemical modelling an initial O/C$^+$ abundance ratio of 1.8 to 2.6 is required to achieve SO/CS abundance ratios as high as 2–7, at late time chemical equilibrium. In the dense cores present in the compressed ridge this chemical equilibrium would appear much earlier in time than in the region near SVS 13, which has been evacuated by the outflowing gas according to Warin et al. (1996). In the less dense regions the chemistry may not yet have reached a late time equilibrium state and hence the SO/CS abundance ratio still remains below 1. In this scenario we have only used the accelerated chemistry and larger SO/CS abundance ratios appearing at increasing densities (Fig. 10). Higher ionization levels, as expected near YSO's, would speed up the chemical evolution, but also could decrease the late time SO/CS abundance ratio (Fig. 11). There is in fact X–ray emission associated with the infrared source SVS 16 (Preibisch et al. 1998), in our map close to the "edge" of the dense region. As discussed in Sect. 4.1 there are also other processes which could modify the chemical evolution such as increased ionization by the UV radiation from newly born stars.

4.1.2. Orion A

This well–studied molecular cloud exhibits the lowest SO/CS abundance ratio in our sample, only 0.1–0.5. We could propose that the Orion A region is much younger (less chemically evolved) than most molecular clouds in our sample, but this seems impossible in view of the rich chemistry of the Orion A core regions (cf. Irvine et al. 1987; Sutton et al. 1995). The very low SO/CS abundance ratio appears to be explainable if the initial O/C$^+$ abundance ratio is low (~ 1.3; i.e. C/O ~ 0.75) i.e. a comparatively C rich environment. This is indeed the current case. The CI abundance in Orion A has been observed to be large ([C]/[CO] $\sim 0.05-0.7$: Phillips & Huggins 1981; Tauber et al. 1995; White & Sandell 1995). However, this is not necessarily a confirmation of the high initial C abundance. A high C concentration "today" probably requires a two–phase cloud model with denser clumps embedded in an interclump medium. The remaining free carbon then would mainly reside in the interclump medium, which is more easily penetrated by ionizing UV radiation, while the more evolved chemistry would dominate in the dark, denser cores.

4.2. The SO enhancement in the outflows of Orion A, NGC 2071 and W 49N

Although outflows are present in many of our observed sources, the kinematical evidence thereof is rarely apparent in our SO and CS spectra (at the current sensitivity level). However, e.g. Chernin et al. (1994) and Lefloch et al. (1998) have demonstrated that the outflow contribution dominates in higher excitation lines of SO and CS. The SO/CS abundance ratios are strongly enhanced in the Orion A and NGC 2071 outflows where we estimate the [SO]/[CS] ratios to be about 24 and 2.2, respectively. This should be compared to the ambient cloud abundance ratios of 0.2 for both sources. The very strong SO abundance enhancement in the Orion A outflow was studied in some detail already by Friberg (1984) (cf. Irvine et al. 1987; Sutton et al. 1995). A similarly strong SO abundance increase recently has been observed in the Sgr B2(M) and (N) cores by Nummelin et al. (2000). Such high SO abundance enhancements would be expected in molecular shocks (e.g. Mitchell 1984; Pineau

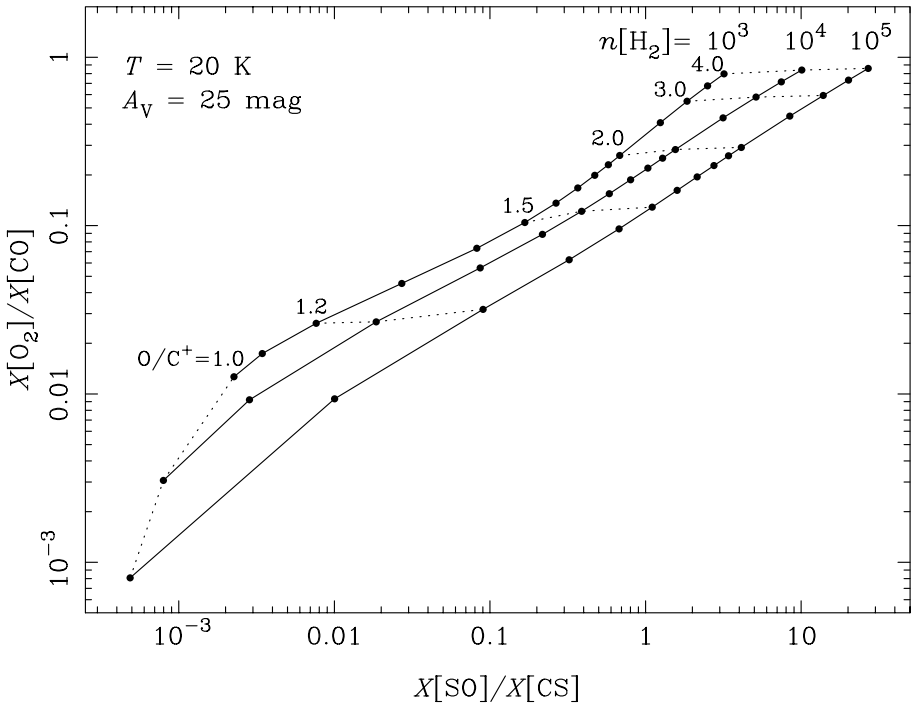

Fig. 22. O_2/CO abundance ratio vs SO/CS at late times for three different H_2 densities. The initial O/C$^+$ ratio varies between 1.0 and 4.0. Note that the O_2/CO ratio is insensitive to variations in H_2 density for O/C$^+ \geq 1.2$. The diagram may be used to *predict* the O_2/CO abundance ratio from the observed SO/CS abundance ratio

des Forêts et al. 1993). The rather high SO/CS abundance ratio in the W 49N core (about 2.2) also may be due in part to the existing massive molecular outflow source (e.g. Downes et al. 1982; Scoville et al. 1986), although this very distant outflow would be unresolved in our 40″ beam and no clear kinematical evidence is apparent in our spectra (see Paper I).

4.3. Predictions of O_2/CO abundance ratios

This question has been adressed in some detail in our chemical modelling, presented in Sect. 3. The initial O/C$^+$ abundance ratio required to produce the observed SO/CS abundance ratio at steady state may also be used to predict the O_2/CO abundance ratios for each source. Such model predictions (for the standard cloud parameters given in Sect. 3) are presented in Fig. 22 for H_2 densities of 10^3, 10^4, and 10^5 cm^{-3}. We note that the O_2/CO abundance ratio is essentially independent of the cloud density (for a fixed O/C$^+$ ratio) while the SO/CS ratio increases markedly with increasing density. This steady state behaviour can also be seen in Fig. 10 and Fig. 13.

In Table 5 we tabulate the range of observed SO/CS abundance ratios in our sources (see Table 3) together with recently published results for Sgr B2, ρ Oph, TMC-1, L134N, and M17 (the references are given in the table). For a few sources, with limited information, only a single SO/CS abundance ratio is given. Since our SO and CS observations mainly probe higher density regions (see Sect. 2.3) we use the $n[H_2] = 10^5$ cm^{-3} model in Fig. 22 together with the highest observed SO/CS abundance ratio to estimate the O/C$^+$ abundance ratio initially required in the various clouds (listed in the fourth column of Table 5). We assume that the initial O/C$^+$ abundance ratio was the same within a cloud (cf. Sect. 4.1). Finally, in the last column of Table 5, the predicted steady state O_2/CO abundance ratio is given. Although the tabulated O_2/CO abundance ratio was calculated using $n[H_2] = 10^5$ cm^{-3} it is also approximately applicable for densities as low as 10^3 cm^{-3} (when the initial [O]/[C$^+$] ratio is known, cf. Fig. 22) if (and only if) the steady state chemistry is reached. However, regions with such low densities are not probed very well by our SO and CS observations.

The estimated initial O/C$^+$ abundance ratios vary from 1.3 (M17) to 2.5 (NGC1333, NGC2071, and L134N). The variation of the predicted O_2/CO abundance ratio is larger: 0.05–0.4. The sources in Table 5 with high [O]/[C$^+$] ratios, and hence high [O_2]/[CO] ratios, should be the most promising candidates for O_2 detection.

4.4. On the detectability of O_2 by the SWAS and Odin satellites

The best limits on the O_2/CO abundance ratio, after 100 hours of SWAS $O_2(N_J = 3_3 - 1_2)$ integration at 487 GHz in several molecular clouds, are reported to be below 0.005 (Goldsmith et al. 1999) which is almost two orders of magnitude lower than our highest predicted ratio (see Table 5 and previous section). Although low beam filling due to the large SWAS antenna beam (HPBW of $3\farcm6 \times 5\farcm0$) may provide a partial explanation, the very low abundance limits observed seem to require an enhanced carbon abundance in the cloud interiors causing efficient destruction of O_2 [cf. Eq (2)]. Turbulent mixing between the outer diffuse regions and the cloud cores has been investigated as a possible cause of C enrichment (Chièze & Pineau des Forêts 1989; Xie et al. 1995). However, such an enrichment simultaneously would reduce the SO abundance, contrary to our observational results (for the high density gas). This failure to simultaneously accomodate a high SO/CS abundance ratio and

a low O_2 abundance appears to indicate a fundamental problem in current chemical models.

To increase the search sensitivity the Odin satellite has been equipped with a low noise HEMT preamplifier for the O_2 $N_J = 1_1 - 1_0$ transition at 119 GHz (HPBW of $9'$). Based on the receiver noise temperatures and O_2 excitation calculations (Bergman 1995; Maréchal et al. 1997b) we estimate, using the appropriate beam sizes, that the Odin sensitivity at 119 GHz will be about an order of magnitude higher than the SWAS sensitivity at 487 GHz. This is valid for small and dense clouds (size $<$ SWAS beam) as well as for more extended (size $\gtrsim$ SWAS beam) and less dense regions.

5. Summary and conclusions

This paper presents our effort to understand whether SO/CS observations could guide the target selection for, and ultimately also support the interpretation of the O_2 observations by the SWAS (Melnick et al. 1997) and Odin (Hjalmarson 1997; Nordh 1997) submillimetre wave spectroscopy satellites. This idea stems from the current knowledge of the dominant source and sink reactions for O_2 and SO, as described in the introduction. To this extent we have embarked on a project which contains **i)** mapping observations of the SO($3_2 - 2_1$) and CS($2 - 1$) transitions, supplemented by ^{34}SO($3_2 - 2_1$) and C^{34}S($2 - 1$) observations in selected core positions, in 19 northern molecular clouds, and **ii)** exploratory gas–phase chemical modelling, based upon infiles from the UMIST RATE95 reaction rate database (Millar et al. 1997). The observational data set has been presented in Paper I. In this paper we have discussed observed SO/CS abundance ratios and have proposed probable interpretations. We have studied how the development of the molecular abundances is influenced by the density, temperature, ionization level (cosmic ray flux or X–ray flux) and by the initial O/C$^+$ and S$^+$ gas phase abundances. We have here presented some modelling results for SO, CS, O_2 and CO as well as for the associated species C$^+$, C, O$^+$, O, H_3^+, OH and H_2O, but only for one cloud temperature (20 K) and for a visual extinction of 25 mag, diminishing the influences of an external UV light field.

Our main conclusions from the observations and the interpretative chemical modelling are:

1. The SO/CS abundance ratios have been observed to vary considerably *within* as well as *between* the molecular clouds in our sample (cf. Tables 2 and 3 and Figs. 1a–1v).
2. The variations of the maximum SO/CS abundance ratio *between* the various clouds fall in the range 0.2–7 and according to our model results most likely are mainly caused by relatively small variations of the initial amounts of gas phase O and C$^+$ in the very young clouds. The required variation of the O/C$^+$ abundance ratio would be only from 1.3 to 2.5, which seems to fall well within the current observational uncertainties. Part of the SO/CS abundance variations between the clouds may also have other reasons as discussed in Sect 4.
3. The appreciable variations of the SO/CS abundance ratio observed within some of the molecular clouds (most remarkably in NGC 1333, NGC 2068 and NGC 2071; cf. Figs. 1d–1e, Fig. 1i, and Fig. 1k) most likely should not be ascribed to variations of the initial O/C$^+$ ratio (since the elemental abundances and depletions are not likely to vary much within a molecular cloud). We here rather propose that we are witnessing varying chemical evolutions caused by local variations of cloud density, or ionization level (presumably due to the X–ray flux from newly formed YSO's). In NGC 1333, and perhaps in NGC 2068 and NGC 2071 as well, such a pronounced density increase may have been invoked by existing molecular outflows [as advocated by Warin et al. (1996) in case of NGC 1333]. Hence it is rather easy to point at probable reasons for the large variations of the SO/CS ratio. On the contrary, the comparatively small variations of this ratio observed in many sources may seem more of a mystery. However, the largest SO/CS ratios and the largest variations appear in the most nearby sources (cf. Table 5). In fact, the large variations seen in NGC 1333 occur on an absolute distance of about 0.34 pc. Variations on this scale cannot be resolved in our $40''$ beam for sources more distant than 2–3 kpc. Thus higher spatial resolution may be required.
4. Only in Orion A and NGC 2071 have our observations clearly revealed the kinematical evidence of molecular outflows. In these cases we have removed a broad gaussian line component from our data, to be able to study the SO/CS abundance variations in the quiescent cloud cores, cf. Paper I and Figs. 1a–1v in this paper. The SO/CS abundance ratios in the Orion A and NGC 2071 outflows are estimated to be 24 and 2.2, respectively. The comparatively large SO/CS abundance ratio (2.2) in the W 49N core position may be partly due to the known massive molecular outflow in this distant source, although we see no clear kinematical evidence thereof.
5. Because of the very similar chemical behaviour of SO and O_2 apparent from our (admittedly crude) modelling results (Figs. 4–15) we advocate that observational studies of the SO/CS abundance variations within and between molecular clouds may be used to find promising targets for detection of the long–sought–for interstellar molecule O_2, see Table 5. High observed SO/CS abundance ratios would be indicative of a large initial O/C$^+$ abundance ratios, which also should lead to large O2 abundances. However, the SWAS O_2 abundance limits recently reported by Goldsmith et al. (1999) are far below our model expectations. Although low beam filling due to the large satellite beam may be of concern, the current chemical models are unable to explain the low abundance of O_2 in regions where the observed SO/CS abundance ratio is high.

Acknowledgements. AN, ÅH, and PB wish to thank the Swedish National Space Board (Rymdstyrelsen) for extensive support. PB and ÅH also acknowledge partial support by the Swedish National Science Research Council (NFR). TJM acknowledges financial support by the UK Particle Physics and Astronomy Research Council (PPARC). We wish to thank the referee L. Pagani and J. Black for constructive criticism which helped to improve the manuscript. Onsala Space Observatory,

the Swedish National Facility for Radio Astronomy, is operated with financial support from NFR and Chalmers University of Technology. This research has made use of the SIMBAD database, operated at CDS, Strasbourg, France. We also made use of the UMIST RATE95 reaction rate database created at UMIST, Manchester, UK.

References

Bergin E.A., Langer W.D., 1997, ApJ 486, 316
Bergin E.A., Langer W.D., Goldsmith P.F., 1995, ApJ 441, 222
Bergin E.A., Goldsmith P.F., Snell R.L., Langer W.D., 1997, ApJ 482, 285
Bergman P., 1995, ApJ 445, L167
Bernes C., 1979, A&A 73, 67
Blake G.A., Sandell G., van Dishoeck E., Groesbeck T.D., Mundy L.G., 1995, ApJ 441, 689
Bohlin R.C., Savage B.D., Drake J.F., 1978, ApJ 224, 132
Casanova S., Montmerle T., Feigelson E.D., Andre P., 1995, ApJ 439, 752
Chernin L.M., Masson C.R., Fuller G.A., 1994, ApJ 436, 741
Chièze J.P., Pineau des Forêts G., 1989, A&A 221, 89
Combes F., Wiklind T., Nakai N., 1997, A&A 327, L17
Downes D., Genzel R., Hjalmarson Å., Nyman L.Å., Rönnäng B., 1982, ApJ 252, L29
Dzegilenko F., Herbst E., 1995, ApJ 443, L81
Edwards S., Snell R.L., 1984, ApJ 281, 237
El-Nawawy M.S., Howe D.A., Millar T.J., 1997, MNRAS 292, 481
Farquhar P.R.A., Millar T.J., Herbst E., 1994, MNRAS 269, 641
Friberg P., 1984, A&A 132, 265
Gear C.W., 1971a, Communications of the ACM 14, 176
Gear C.W., 1971b, Numerical initial value problems in ordinary differential equations. Prentice–Hall
Gerin M., Falgarone E., Joulain K., et al., 1997, A&A 318, 579
Goldsmith P.F., Ashby M.L.M., Bergin E.A., et al., 1999, BAAS 31, 1465
Gottlieb C.A., Gottlieb E.W., Litvak M.M., Ball J.A., Penfield H., 1978, ApJ 219, 77
Green S., 1994, ApJ 434, 188
Heithausen A., Corneliussen U., Grossmann V., 1998, A&A 330, 311
Herbst E., Lee H.-H., 1997, ApJ 485, 689
Hindmarsh A.C., 1972a, Linear multistep methods for ordinary differential equations. Method formulations, stability, and the methods of Nordsieck & Gear. Lawrence Livermore Laboratory Report UCRL–51186 Rev. 1
Hindmarsh A.C., 1972b, Construction of mathematical software. Part III. The control of error in the Gear package for ordinary differential equations. Lawrence Livermore Laboratory Report UCID–30050 Part 3
Hindmarsh A.C., Gear C.W., 1974, Ordinary differential equation system solver. Lawrence Livermore Laboratory Report UCID–30001 Rev.
Hjalmarson Å., 1997, In: Latter W.B,, Radford S.J.E., Jewell P.R., Mangum J.G., Bally J. (eds.) CO: Twenty–five years of millimeter–wave spectroscopy. IAU Symposia 170, Kluwer Academic Publishers, Dordrecht, Netherlands, p. 227
Irvine W.M., Goldsmith P.F., Hjalmarson Å., 1987, In: Hollenbach D.J., Thronson H.A. (eds.) Interstellar Processes. Reidel, Dordrecht, p. 561
Jennings R.E., Cameron D.H.M., Cudlip W., Hirst C.J., 1987, MNRAS 226, 461
Krolik J.H., Kallman T.R., 1983, ApJ 267, 610
Langer W.D., Graedel T.E., Frerking M.A., Armentrout P.B., 1984, ApJ 277, 581
Langer W.D., Castets A., Lefloch B., 1996, ApJ 471, L111
Le Bourlot J., Pineau des Forêts G., Roueff E., 1995, A&A 297, 251
Lee H-H., Bettens R.P.A., Herbst E., 1996, A&AS 119, 111
Lefloch B., Castets A., Cernicharo J., Loinard L., 1998, ApJ 504, L109
Lepp S., Dalgarno A., 1996, A&A 306, L21
Liseau R., Sandell G., Knee L.B.G., 1988, A&A 192, 153
Liseau R., Lorenzetti D., Molinari S., et al., 1995, A&A 300, 493
Lucas R., Liszt H., 1998, A&A 337, L246
Maréchal P., Pagani L., Langer W.D., Castets A., 1997a, A&A 318, 252
Maréchal P., Viala Y.P., Benayoun J.J., 1997b, A&A 324, 221
Melnick G.J., Dalgarno A., Erickson N.R., et al., 1997, In: Wilson A. (ed.) ESA Symposium SP–401: The Far InfraRed and Submillimetre Universe. ESA Publications Division, ESTEC, Noordwijk, The Netherlands, p. 189
Melnick G.J., Stauffer J.R., Ashby M.L.N., et al., 1999, BAAS 194, 4708
Millar T.J., Farquhar P.R.A., Willacy K., 1997, A&AS 121, 139
Mitchell G.F., 1984, ApJ 287, 665
Mundy L.G., Snell R.L., Evans N.J., Goldsmith P.F., Bally J., 1986, ApJ 306, 670
Nilsson A., 1999, Technical Report No. 304L, Lic. Eng. Thesis, Chalmers University of Technology, Göteborg, Sweden
Nilsson A., Bergman P., Hjalmarson Å., 2000, A&AS 144, 1 (Paper 1)
Nordh L., 1997, In: Wilson A. (ed.) ESA Symposium SP–401: The Far InfraRed and Submillimetre Universe. ESA Publications Division, ESTEC, Noordwijk, The Netherlands, p. 195
Nummelin A., Bergman P., Hjalmarson Å., et al., 2000, ApJS, in press
Olofsson G., Pagani L., Tauber J., et al., 1998, A&A 339, L81
Olofsson H., Elldér J., Hjalmarson Å., Rydbeck G., 1982, A&A 113, L1
Patel N.A., Goldsmith P.F., Snell R.L., Hezel T., Xie T., 1995, ApJ 447, 721
Phillips T.G., Huggins P.J., 1981, ApJ 251, 533
Pineau des Forêts G., Roueff E., Schilke P., Flower D.R., 1993, MNRAS 262, 915
Pratap P., Dickens J.E., Snell R.L., et al., 1997, ApJ 486, 862
Preibisch T., Neuhaeuser R., Stanke T., 1998, A&A 338, 923
Scoville N.Z., Sargent A.I., Sanders D.B., et al., 1986, ApJ 303, 416
Snell R.L., Edwards S., 1982, ApJ 259, 668
Snell R.L., Mundy L.G., Goldsmith P.F., Evans N.J., Erickson N.R., 1984a, ApJ 276, 625
Snell R.L., Scoville N.Z., Sanders D.B., Erickson N.R., 1984b, ApJ 284, 176
Spitzer L., 1978, In: Physical processes in the interstellar medium.
Sutton E.C., Peng R., Danchi W.C., et al., 1995, ApJS 97, 455
Swade D.A., 1989a, ApJS 71, 219
Swade D.A., 1989b, ApJ 345, 828
Tauber J.A., Lis D.C., Keene J., Schilke P., Büttgenbach T.H., 1995, A&A 297, 567
Taylor S.D., Morata O., Williams D.A., 1998, A&A 336, 309
Turner B.E., 1991, ApJS 76, 617
Turner B.E., Chan K.-W., Green S., Lubowich D.A., 1992, ApJ 399, 114
Warin S., Castets A., Langer W.D., Wilson R.W., Pagani L., 1996, A&A 306, 935
White G.J., Sandell G., 1995, A&A 299, 179
Williams D.A., 1993, In: Millar T.J., Williams D.A. (eds.) The Graduate Series in Astronomy. IOP Publishing, p. 143
Wilson T.L., Rood R., 1994, ARA&A 32, 191
Xie T., Allen M., Langer W.D., 1995, ApJ 440, 674